This is a repository copy of *Graphene nanoplatelets/Ni-Co-Nd spinel ferrite composites with improving dielectric properties*.

Graphene nanoplatelets/Ni-Co-Nd spinel ferrite composites with improving dielectric properties

Kiran Mehmood[a], Atta Ur Rehman[a], Nasir Amin[a], N. A. Morley[b], Muhammad Imran Arshad[a]*,

[a]*Department of Physics, Government College University, Faisalabad, 38000, Pakistan.*

[b]*Department of Materials Science and Engineering, The University of Sheffield, UK, S1 3JD.*

*Corresponding Author: miarshadgcuf@gmail.com

Abstract

Due to their low cost, easy preparation, and outstanding electrical, dielectric, and magnetic properties, spinel ferrites are of enormous scientific and technological importance. Moreover, graphene nanoplatelets (GNPs) are an excellent supporting material for the construction of a wide range of composites. The sol-gel auto combustion (SGAC) route was used to prepare $Ni_{0.5}Co_{0.5}Fe_{1.97}Nd_{0.03}O_4$ (NCNF) ferrite and their composites with GNPs. Single-phase structures were found by X-ray diffraction (XRD) analysis and the crystallite size increased with the insertion of GNPs into the NCNF sample. Raman spectra also confirmed the spinel structure of the ferrites and supported the existence of graphene in the composite. Micrographs indicate that agglomeration decreased in all the samples. It was found for the NCNF/2.5wt%GNPs composite, the energy bandgap was 1.90 eV, while the temperature coefficient of resistance (TCR) had a value of -4.27 K^{-1} and the values of the dielectric constant and quality (*Q*) factor were a maximum. Moreover, the dielectric tangent loss was minimum, and magnetic tangent loss was maximum for the NCNF/2.5wt%GNPs composite. A saturation magnetization of 108.83 emu/g and 24.06 GHz microwave frequency were observed for NCNF/2.5wt%GNPs composite. Therefore, the composite NCNF/2.5wt%GNPs had improved dielectric characteristics making them a promising material for a variety of applications, including microwave frequency operating devices, bolometric devices, and microwave absorbing materials.

Keywords: Sol-gel auto combustion; ferrites; graphene; temperature coefficient of resistance; dielectric.

1. Introduction

Graphene nanoplatelets (GNPs) offer a wide range of applications in condensed matter physics, material science, microwave absorption, and electronics due to their unique two-dimensional (2D) structure [1-6]. Graphene nanoplatelets exhibit high surface area [7],

antibacterial properties [8], effective electron mobility, and excellent electrical with chemical properties. These properties of graphene provide support for nanoparticles in the formation of composites [9]. Moreover, graphene has a high dielectric property, which causes poor impedance and low absorption characteristics along with agglomeration. Graphene's agglomeration formation problem can be overcome by the use of rare-earth (RE) ions substituted ferrites because REs ions act as spacers for the graphene nanosheets [10].

Spinel, garnet, hexagonal, and ortho-ferrites are the different categories of ferrites based on their structure. AB_2O_4 is the general formula for spinel ferrites (SFs), where "A" may be divalent ions or a combination of different divalent ions, and "B" indicates trivalent and RE ions. The behaviour of these materials can be tuned by the selection of some physical conditions such as synthesis method, precursors, dopant metal, chemical composition, and calcination temperature [11-15]. Ni-Co SFs have high symmetry and low magnetocrystalline anisotropy [10]. It was reported that the addition of RE ions into SFs causes deformation of the structure and thus modifies their electrical and chemical properties [16-18]. Therefore, researchers have paid great attention to the preparation of RE substituted SFs to enhance their properties. Kokare et al., [19] used a sol-gel auto combustion process to synthesize the $Ni_{0.5}Co_{0.5}Fe_2O_4$ (NCF) sample and reported a 33.38 nm crystallite size. Farooq et al., [20] also prepared an NCF sample and claimed the lattice constant was 8.3490 Å. The structural and optical parameters of the NCF sample were reported by Pawar et al., [21]. The lattice constant was observed at 8.3449 Å and the energy bandgap was 2.72 eV along with the crystallite size of 33.50 nm.

Graphene (G) and its derivative materials have attracted researcher's interest due to their unique properties and practical applications. Graphene may also be combined with a variety of inorganic and organic functional components to create composites, making it a multipurpose material [22]. Increasing the concentration of graphene nanoplatelets (GNPs) creates agglomerates, with lower dielectric losses, higher dielectric constant, and inhomogeneities [3]. Because of their high density, the use of SFs as microwave absorbing materials (MAMs) is limited and demands the combination with GNPs as light materials for the MAMs applications. Conduction loss contributes to semicircle distortion by causing a linear portion to appear in the Cole-Cole plots of semicircles in $(MnNiCu)_{0.9-x}Co_xZn_{0.1}Fe_2O_4$/G composites [6]. Improved absorption characteristics of $MgFe_2O_4$ (MFO)/G hybrids composites were the result of three factors: (1) The 2D planar conductive graphene produced a conductive network in the materials, resulting in a high tangent loss, (2) the composite's structural stability was improved by the uniform distribution of MFO nanorods on the graphene sheet, which was advantageous for electromagnetic wave attenuation. (3) Finally, due to the difference between

2

graphene and MFO nanorods in permittivity, interface scattering would be produced, resulting in more efficient absorption [3-6]. The efficient complementation of permeability and permittivity results in excellent microwave absorption, while both magnetic and dielectric loss contributes to microwave absorption [23]. $Ni_{0.5}Co_{0.5}Fe_2O_4$/G composites with outstanding microwave absorption were prepared using a hydrothermal route and results showed that adding graphene to an appropriate range can significantly improve microwave absorbing performance, with magnetic loss contributing to the majority role in microwave absorption of composites [24]. This improved absorption performance could be attributed to interfacial polarization and a good impedance match resulting from the dielectric's unique pore configuration [25]. The grain size was reduced when $CoFe_2O_4$ blended with GNPs and the permittivity varies inversely with grain size, although the loss (imaginary permittivity) obtained is relatively less. For devices that operate in the microwave or radio frequency range, these properties are critical. As a result, the ferrite's substantially lower dielectric constants allow them to be used at high frequencies [26]. When GNPs were added in $Ni_{0.4}Zn_{0.6}Fe_2O_4$ ferrite, the permittivity (real and imaginary part) and imaginary parts of complex permeability of composites were significantly improved, indicating that higher magnetic and dielectric loss tangent of composites were achieved [5]. Qamar *et al*., [27] reported that the lattice constant for $Ni_{0.5}Co_{0.5}Ce_{0.2}Fe_{1.8}O_4$ (NCCF) ferrite and $Ni_{0.5}Co_{0.5}Ce_{0.2}Fe_{1.8}O_4$/G composite was 8.651 Å and 8.846 Å, respectively. They added 20wt% graphene to the NCCF sample and observed an increase in the lattice constant due to the addition of graphene. The increase in lattice constant may be due to the incorporation of graphene [27-29].

However, few studies were published that use SFs blended with graphene nanoplatelets, which may have a unique improvement in magnetic and dielectric properties due to the combination of ferrite's remarkable magnetic properties and graphene's excellent electrical conductivity. The newly synthesized novel composites are expected to have a significant dielectric improvement and could be used in high-frequency devices.

Radiofrequency plasma method [30], co-precipitation method [31], reverse microemulsion route [32], mechanical milling [33], sol-gel auto combustion (SGAC) method [34], and hydrothermal method [35], and are some of the methods used to prepare graphene composites. Therefore, in this article, we report on $Ni_{0.5}Co_{0.5}Fe_2O_4$ (NCF), $Ni_{0.5}Co_{0.5}Nd_{0.03}Fe_{1.97}O_4$ (NCNF), $Ni_{0.5}Co_{0.5}Fe_{1.97}Nd_{0.03}O_4$/2.5%GNPs (NCNF/2.5wt%GNPs), and $Ni_{0.5}Co_{0.5}Fe_{1.97}Nd_{0.03}O_4$/5%GNPs (NCNF/5wt%GNPs) composite synthesized *via* SGAC technique and investigate their structural, morphological, optical, electrical, dielectric, and magnetic properties.

3

2. Experimental Method

2.1 Materials and samples preparation method

The precursors Co $(NO_3)_2$. $6H_2O$ (98.50%), Fe $(NO_3)_3$. $9H_2O$ (99.95%), Nd $(NO_3)_3$. $6H_2O$ (99.99%), Ni $(NO_3)_2$.$6H_2O$ (99.99%), and graphene nanoplatelets (GNPs) were used to prepare the NCF, NCNF, NCNF/2.5wt%GNPs, and NCNF/5wt%GNPs composites by the SGAC method The citric acid was used as a combustible agent for the as-synthesized composites powder. Metal nitrates to citric acid molar ratio were kept at 1:1.2. The GNPs were taken as 2.5wt% and 5wt% with an NCNF sample to prepare composites of NCNF and GNPs.

The solution of all nitrates was mixed and stirred for 10 minutes on a magnetic stirrer. GNPs solution was added to the metal nitrates solution. Furthermore, the solution of citric acid was added and sonicated for 30 mins to form a homogeneous solution. This solution was kept at a magnetic stirrer with 50 rev/min speed and ammonia was added dropwise to obtain a pH 7. After that heat was turned on while continuously stirring. The heating and stirring were sustained till the formation of viscous gel at 353 K. This gel was heated at 573 K to get fluffy powder by auto combustion. This powder was then grounded and calcinated at 1123 K for 5 hrs. The obtained powder was again ground and used for the different characterization techniques. The complete process is demonstrated in Fig. 1.

2.2 Characterization used

Using Cu K_α radiation with λ = 0.1542 nm, X-ray diffraction (XRD) was performed with Bruker D8 Advance X-ray diffractometer. The synthesized sample's structure was also confirmed using Raman spectroscopy using a 532.8 nm laser excitation. The morphology of the synthetic materials was studied using Scanning electron microscopy (SEM, NOVA NANOSEM 430). The energy bandgap was estimated using UV–visible spectroscopy. In this study, the electrical characteristics were measured using a KEITHLEY Model 2401 Sourcemeter, two probes I–V measurement meter. At room temperature (RT), dielectric measurements were obtained using the IM3530 series LCR Meter. At room temperature (RT), a vibrating sample magnetometer (VSM) was used to measure the sample's magnetic properties.

3. Results and their discussion

3.1 Structural analysis

XRD spectra of the as-prepared ferrites and composites are depicted in Fig. 2(a). The diffraction planes (220), (311), (222), (400), (422), and (511) indicate the spinel matrix. The appearance of a large peak in the diffraction plane (311) showed the presence of spinel phase structure in the samples. A small peak shift was observed in the (311) plane towards a greater

diffraction angle in the NCNF sample due to the substitution of Nd^{3+} into the NCF sample as depicted in Fig. 2(b). It was also observed from Fig. 2(c) that with the addition of 2.5wt% GNPs and 5wt% GNPs into the NCNF spinel matrix, the peak (311) shifts toward the smaller diffraction angle. Fig. 2(d) shows the XRD spectra of pure GNPs and two peaks labeled with planes (022) and (044) are observed. However, the composites with the addition of GNPs showed similar patterns to the NCNF sample (Fig. 2(a)). This may be due to the low crystalline matrix of GNPs [27].

The lattice parameter values are given in Table 1. The lattice constant (*a*), interplanar distance (*d*), and unit cell volume (*V*) were determined [15, 36]. The value of interplanar spacing was reduced from 2.517 Å to 2.515 Å with the substitution of Nd^{3+} ion into the NCF spinel matrix. Moreover, with the doping of GNPs in the NCNF spinel lattice, the interplanar spacing was increased from 2.518 Å to 2.531 Å. The unit cell volume and lattice constant have a similar trend to interplanar spacing (as shown in Fig. 3(a)). The reduction in the lattice parameters was observed due to the substitution of Nd^{3+} (0.983 Å) with Fe^{3+} (0.64 Å). Another reason for the reduction in lattice parameters might be the higher ionic radius of Nd^{3+} ions, which causes lower degrees of lattice fringe alignment and lattice distortion [37]. However, the increase in the lattice parameters was due to the addition of GNPs in the NCNF spinel lattice. The change in structural parameters was also observed by different researchers and reported that the structural parameters were varied due to the incorporation of graphene in the spinel structure [27-29]. The Scherer formula was used to calculate crystallite size (*D*), lattice strain (*ε*), and dislocation line density (*δ*) were also determined [15, 38]. The full width at half maxima (FWHM) values were given in Table 1. The size of the crystallites in these samples increased from 33.49 nm to 39.55 nm. The samples *versus* FWHM and crystallite size were depicted in Fig. 3(b). The doping of Nd^{3+} ions increased the crystallite size of NCF samples, which was further enhanced by the insertion of GNPs in the NCNF sample and a similar trend was observed in the literature [39]. The dislocation line density was reduced with the doping of Nd^{3+} ion in the NCF sample and GNPs in the NCNF spinel lattice (trend as shown in Fig. 3(c)). With the doping of Nd^{3+} ions in the NCF sample, the strain was also reduced to 0.339. The addition of GNPs in the NCNF spinel lattice resulted in a small decrease in lattice strain (0.301) and graphically depicted in Fig. 3(c). In short, it was found that adding GNPs to the NCNF sample changed its structure, shape, and geometry.

3.2 Raman analysis

Raman spectra are commonly used to explain the vibrational dynamic in terms of normal modes inside the two sub lattice sites i.e., tetrahedral and octahedral sites within the

spinel structure. The tetrahedral (A) site is a tetrahedron composed of the cation at the center of a cube and four oxygen atoms in the nonadjacent corners; the octahedral (B) site is an octahedron consisting of a cation surrounded by six oxygen atoms, two along each dimensional axis [40].

The Raman spectra of pure GNPs are depicted in Fig. 4(a), and the Raman spectra of all ferrites and composites are shown in Fig. 4(b). The modes are given in the relation: $A_{1g}(R) + E_g(R) + T_{1g} + 3T_{2g}(R) + 2A_{2u} + 2E_u + 5T_{1u}(IR) + 2T_{2u}$ all belong to the SFs crystal structure with the O7h space group. Raman (R) active modes include $3T_{2g}(R)$, $E_g(R)$, and $A_{1g}(R)$. T_{1u} is an infrared (IR) active mode, whereas $2T_{2u}$, $2E_u$, $2A_{2u}$, and T_{1g} are symmetry vibration modes. Table 2 summarized the natural frequencies of the Raman active modes. The Raman modes of the SFs, as well as two bands at 1600 cm^{-1} (G-band) and 1300 cm^{-1} (D-band), correspond to the free-defect and disordered regions of graphene, which is seen in the NCNF/2.5wt%GNPs and NCNF/5wt%GNPs composites.

3.3 Morphological analysis

The surface morphology of all the ferrites and composites is presented in Fig. 5(a-d). Clusters of particles in NCF and NCNF samples were seen in Fig. 5(a-b), respectively. The particles of the NCF sample were agglomerated as depicted in Fig. 5(a). In the NCNF sample, substitutions of Nd^{3+} ions in the NCF spinel matrix decreased agglomeration (Fig. 5(b)). The increase in the crystallite size with the doping of Nd^{3+} ions in the NCF spinel lattice was established by XRD analysis (Table 1). Therefore, the greater the crystallite size, the less will be the agglomeration. The micrographs of NCNF/2.5wt%GNPs and NCNF/5wt%GNPs composites are shown in Fig. 5(c-d). The inclusion of GNPs in the NCNF sample also decreased agglomeration, as seen in Fig. 5(c-d). The high tendency of graphene to form agglomeration was prevented by the combination with the ferrites and reduced the agglomeration of the graphene-based ferrites composites [10, 22].

3.4 Energy bandgap analysis

The Tauc plots of all the samples are depicted in Fig. 6(a-d), and the energy bandgap (E_g) was calculated. It is clear from Fig. 6(a-d) that the "E_g" has values of 3.01 eV, 1.97 eV, 1.90 eV, and 2.30 eV for NCF, NCNF, NCNF/2.5wt%GNPs, and NCNF/5wt% GNPs composites respectively. The un-doped NCF sample has the largest energy bandgap because of the orbital overlap between the O^{2-}p and Fe-3d energy states. The energy bandgap is reduced with Nd^{3+} doping in the NCF sample. As a result of the interaction between this 4f energy state and the valence state O^{2-}p orbital, charge migration from Nd^{3+} energy levels to the NCF sample

conduction band occurs [41]. With the addition of GNPs in the NCNF sample, the value of "E_g" was 1.90 eV for 2.5wt%GNPs composite, and for 5wt%GNPs composite the "E_g" was 2.30 eV.

3.5 Electrical analysis

One of the most powerful techniques for explaining the electrical behaviour of ferrite and its derivatives is temperature-dependent resistivity (ρ) measurement. Arrhenius plots (10^3/T *versus* log ρ) for the as-synthesized ferrites and composites are depicted in Fig.7. It is clear from Fig. 7 that all the samples have two distinct regions based on transition temperature called the Curie temperature (T_C). The Curie temperature of the as-prepared samples is the temperature at which a sharp change in the magnetic properties is observed and separates the ferro region (magnetic moment is in order state) and para region (magnetic moment is in disorder state) [14]. The ferro region lies below "T_C" and the para region lies above "T_C". The semiconducting nature was demonstrated by a reduction in resistivity with increasing temperature for all samples. It could be because when the temperature rises, the activated drift mobility of electric charge carriers increases. The electronic conduction in ferrites is dominated by electron hopping between the same ions with multivalence states (such as Fe^{3+} and Fe^{2+} ions), which is dispersed arbitrarily among lattice sites, according to Verwey's hopping mechanism [42]. Also, it was observed from Fig.7 that the resistivity is high, in the order of $10^5 - 10^8$ Ω. This may be due to the poor conductivity of SFs, which conduct by the hopping of electrons between ferric (Fe^{3+}) and ferrous (Fe^{2+}) ions at *B*-sites.

$$Fe^{2+} \quad \rightarrow \quad Fe^{3+} + e^-$$
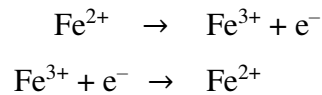$$Fe^{3+} + e^- \quad \rightarrow \quad Fe^{2+}$$

Fig.8(a-c) shows the concentration *versus* resistivity plots at different temperature ranges. Fig.8(a) represents low-temperature region concentration *versus* resistivity and observed that in this region the resistivity was maximum for NCNF/2.5wt%GNPs composite. Fig.8(b-c) revealed that the resistivity has the maximum value for the NCNF sample in the moderate and high-temperature regions.

The slope of the plots as shown in Fig. 7 (Arrhenius plots) was used to calculate the activation energy ($\Delta E = E_p - E_F$) *via* equations: $E = 2.303 \times k_B \times 10^3 \times$ slope (eV) [43, 44] where "E_p" is the activation energy of the paramagnetic region, "E_F" represents activation energy of the ferromagnetic region, and "k_B" Boltzmann constant (8.602×10^{-5} eV/K). The activation energy is 0.7451 eV, 0.8111 eV, 0.8906 eV and 0.7935 eV for NCF, NCNF, NCNF/2.5wt%GNPs, and NCNF/5wt%GNPs composites, respectively (as represented in Fig. 9).

Temperature coefficient of resistance (TCR) percentage values were determined for all the samples using temperature (T) dependent resistivity (ρ) [42]. TCR% values for all samples in the range of 313 K to 543 K are depicted in Fig. 10(a-d). All samples showed a peak in the temperature dependence of the TCR curves, and the peaks were observed at 382 K in all the samples. The peak position of temperature *versus* TCR% plots was -3.79 K^{-1}, -4.04 K^{-1}, -4.27 K^{-1}, and -4.40 K^{-1} for NCF, NCNF, NCNF/2.5wt%GNPs, and NCNF/5wt%GNPs composites, respectively. Time and sintering temperature influence the peak value of TCR% [42]. Due to the high value of TCR, this research suggests that as-prepared ferrites and composites may be useful for bolometric device applications. Fig.11(a) represents low-temperature region (313 K – 343 K) samples *versus* TCR%. It was observed that in this region the TCR% was maximum for the NCF sample and minimum value for composite NCNF/5wt%GNPs. It was found that the samples have positive values of TCR% at low temperatures (as seen in Fig.10 and also in Fig.11(a)). Fig.11(b) indicates the negative values of TCR% for moderate temperature regions (353 K – 433 K) for the as-prepared ferrites and composites. In the high-temperature region (523 K – 543 K), the negative TCR% was maximum for the NCF sample and minimum value for composite NCNF/5wt%GNPs.

3.6 Dielectric analysis

The frequency *versus* dielectric constant (ε') plots are shown in Fig. 12(a) and it was observed that as the frequency increased, the charge carriers accumulated at the boundaries could not continue to follow the field variation. Therefore, the dielectric constant remains constant at a higher frequency. A greater dielectric constant of the composites was observed as compared to the pure NCF sample, as illustrated in Fig. 12 (a). The variation in the dielectric constant with frequency shows the dispersion caused by Maxwell-Wagner type interfacial polarization, which is in accordance with Koop's phenomenological theory [45]. At low frequency, the large value of the dielectric constant revealed that all types of polarization exist including atomic, electronic, interfacial, and dipolar polarization. The mechanism of polarization in ferrites is the same as that of conduction, i.e., charge carriers hopping between multivalence ions of the same element while because graphene improved conductivity, the dielectric constant was also increased. Overall, graphene enhances the dielectric constant values. Fig. 12 (b) depicts the log of frequency *versus* dielectric loss (ε''). In an applied electrical field dipole orientation of dielectric material can be caused by the absorption of energy, this loss of energy is well-defined by dielectric loss. The pure NCF sample has a high dielectric loss while the NCNF/2.5wt%GNPs composite has a low dielectric loss (as shown in

Fig. 12 (b)). The loss of tangent (tan δ_e) for all of the as-prepared samples is shown in Fig. 12 (c). The dielectric loss tangent is the dissipated energy in a dielectric material due to different phenomena including electrical conduction, dielectric relaxation, and domain wall dielectric resonance [29, 46, 47]. Due to Maxwell–Wagner polarization, the loss tangent decreased with enhancing frequency and at a high-frequency tangent, the loss remains constant. The loss tangent has high values at low frequency, but as the frequency rises, the tangent is substantially reduced. The loss tangent for the pure NCF sample is higher than the NCNF sample while by adding the GNPs in the NCNF sample the tangent loss was reduced for 2.5wt%GNPs and for 5wt%GNPs the tangent loss increased as compared to the pure NCF and Nd^{3+} ion-doped NCF sample. The composite has a relatively low loss tangent that's because the real permittivity has always been high [48]. It could be owing to graphene's high electrical conductivity [49]. The tangent loss values are affected by sintering temperature, structural uniformity, and iron ion concentration [29].

The variation of frequency *versus* ac conductivity (σ_{ac}) is similar for all the samples and exhibits semiconducting behaviour well known for ferrites (as shown in Fig. 12 (d)). It was clear from Fig. 12 (d) that adding GNPs reduced the "σ_{ac}" at the low percentage of graphene (2.5wt%GR) while for the high percentage of graphene (5wt%GNPs) the "σ_{ac}" values were increased as compared to pure NCF and Nd^{3+} ions doped NCF samples. Furthermore, Koop's theory [42] that defined the ferrite's heterogeneous structure consisting of conducting grain regions separated by poorly conducting grain boundary regions explains the observed ac conductivity frequency dependence. The ac conduction is done through a charge carrier hopping mechanism [42] between cations with various valences present at the same site. Charge carriers will accumulate at the grain boundary due to the differential in conductivity between the two regions, resulting in interfacial polarization. Furthermore, at lower frequencies, the resistant grain boundaries are thought to be the most important functional components of conduction, whereas, at higher frequencies, the more conductive grains are the key contributors to conduction [50].

The relation between the rate of dissipated energy and the stored energy is valuable to predict the efficiency of different electrical components as well as devices. This rate of both energies defines the Quality (*Q*) factor of that device. The *Q* factor of as-prepared samples is shown in Fig. 13. The value of the Q factor is maximum for NCNF/2.5wt%GNPs composite and minimum for NCNF/5wt%GNPs composite.

Fig.14(a-d) depicted Cole-Cole plots showing the variation of complex permittivity for all the ferrites and composites. At lower frequencies, a linear behaviour was observed, and the

9

linear response slowly turns to a semi-circle arc at higher frequencies, indicating that the as-synthesized ferrites and composites are semi-conductive at higher frequencies and insulating at lower frequencies. Grains are electrically less resistive than the grains boundaries due to crystalline characteristics i.e., grains having low resistance and grain boundaries having high resistance. Koop's theory was confirmed by Maxwell–Wagner, who stated that greater resistance regions have interfacial polarization because of charge accumulation at grain boundaries.

Two parallel components are coupled in series in an electrical circuit model and can thus be used to understand the existence of high and low impedance semi-circular arcs. The combined effect of grain boundary and grain resistance will be the circuit's overall impedance. As a result, the low impedance semicircular arcs are attributed to grain boundary resistance, and the high-frequency semicircular arcs are attributed to bulk impedance [51]. With the increased radius of the semi-circle with increasing dopant concentration, the material's *ac* conductivity has increased. Fig. 15(a) represents the log of frequency *versus* the real part of impedance (Z′) of as-prepared samples. It is revealed from Fig. 15 (a) that impedance decreases with increasing frequency then becomes constant at a higher frequency, and has high values at low frequency. This indicates that the as-prepared ferrites and composites are used as dielectrics in low-frequency devices. The impedance has no significant value after about 10^5 Hz, indicating that the conduction mechanism has become dominating in the as-prepared materials due to electron hopping at high frequencies. Space charge polarization and low conductivity in the material results in high impedance values in all samples at low frequencies. As the frequency rises, the transmission in the material increases, leaving only space charge polarization in the higher frequency regions [52, 53]. Fig. 15(b) shows the plots of the log of frequency against the imaginary part of impedance (Z″). It was found that when frequency increases, the imaginary part of impedance decreases. In all samples, the constant values of the imaginary part of impedance at the higher frequency domain are because of space charge polarization, just as they were in the real part of the impedance. In the high-frequency domain, this continuous behaviour demonstrates that the real and imaginary impedances behave independently of frequency.

The Nyquist plot is a graph that shows the change in real *versus* imaginary parts of impedance as shown in Fig. 16 for all the ferrites and composites. A Nyquist plot is formed of one or more semicircles. Semicircles, on the other hand, may not always be completed. At low frequencies, the semicircle can be attributed to the grain boundary, whereas at high frequencies,

the second semicircle can be assigned to grain contribution. Because both semicircles are present, the dielectric process is dependent on two relaxation processes.

The toroid-shaped sample was wound with four rounds of enameled copper wire, and the inductance (L_S) was determined at RT. The real part of initial permeability was calculated using [54]; $\mu' = L_S/L_o$, where $L_o = \mu_o hN^2/2\pi$ ln r_o/r_i is coil inductance without sample core, while h, N, r_o, and r_i represent the thickness, number of turns of the coil, outer and inner radius of the toroid-shaped sample, respectively. The frequency-dependent real part of initial permeability (μ') spectra is shown in Fig. 17(a). It was observed from Fig. 17(a) that the real part of initial permeability remained constant at low frequency and was reduced sharply with an increase in the frequency at high frequency. As shown in Fig. 17(b), the spectra of the imaginary part of complex permeability ($\mu'' = \mu' \times \tan \delta_m$) [54] with respect to the log of frequency. For all the samples, we have some oscillating response at a lower frequency, which becomes stationary at higher frequencies. The as-prepared ferrites and composites had a sharp decrease until becoming independent of higher frequencies. The as-synthesized ferrites and composites response is dominated at higher frequencies. The magnetic tangent loss (tan δ_m) [55] of as-prepared ferrites and composites will be significantly improved in the low-frequency domain with a graphene content, as shown in Fig. 18. It was noted that the magnetic tangent loss was decreased with frequency and had a maximum value for composite with GNPs concentration of 2.5wt%. The major determinants of absorption capabilities are dielectric and magnetic tangent losses. The dielectric tangent loss is proportional to the dielectric loss and describes how energy from an external electric field is dissipated as heat and motion. The magnetic tangent loss is a measure of the energy loss inside a magnetic material due to the phase delay between the applied and induced magnetic fields; it is also known as the magnetic loss factor [56]. Furthermore, the dielectric tangent loss was minimum, and magnetic tangent loss was maximum for the composite with 2.5w% GNPs content, while the magnetic tangent loss of the composites is significantly higher than the dielectric tangent loss, indicating that, both contribute to the microwave absorption of the composites.

Fig. 19(a) clearly showed that the dielectric constant and quality factor has maximum values, while Fig. 19(b) the *ac* conductivity, and dielectric tangent loss has minimum values, while magnetic loss has maximum value for NCNF/2.5wt%GNPs composite at 15 kHz. Therefore, these results indicate the NCNF/2.5wt%GNPs composite for microwave absorbing materials.

3.7 Hysteresis loop analysis

The magnetic hysteresis (*M-H*) loops of all the ferrites and composites were recorded at RT and are shown in Fig. 20 and applied field *versus* microwave frequency as shown in Fig. 21. The magnetic properties are affected by the synthesis method, sintering temperature, and cation replacement. Table 3 summarized the magnetic parameters. The samples *versus* changes in saturation magnetization (M_S), remanence (M_r), coercivity (H_C), and squareness ratio (M_r/M_s) plots were depicted in Fig. 22(a-b). The value of "M_S" was decreased from 117.73 emu/g to 114.05 emu/g with the addition of Nd^{3+} ions in NCF samples. The value of "M_S" was 108.83 emu/g for NCNF/2.5wt%GNPs composite and NCNF/5wt%GNPs composite has an "M_S" value of 93.97 emu/g (Fig. 22(a)). The remanence decreased for the ferrite samples as well as for composite with graphene nanoplatelets content of 2.5wt%GNPs and the increase for 5wt%GNPs composite as compared to the pure NCF sample (Fig. 22(a)). The coercivity of spinel ferrites depends on crystal structure, particle size, morphology, anisotropy, and strain [46]. The coercivity has a minimum value for the NCNF sample, while it increased from 250.61 Oe to 397.41 Oe as the GNPs concentration increased from 2.5wt% to 5wt% and the squareness ratio has a smaller value for the NCNF/5wt%GNPs composite compared to NCNF/2.5wt%GNPs composite (Fig. 22(b)). The magnetocrystalline anisotropic constant ($K = \frac{H_c \times M_s}{0.96}$), and initial permeability ($\mu_i = \frac{M_s^2 \times D}{K}$) were determined [46] and graphically represented in Fig. 22(c). The minimum anisotropy constant and maximum initial permeability were observed for the NCNF sample. The doping of Nd^{3+} ions in NCF samples decreased the saturation magnetization and other magnetic properties. It may be due to the replacement of Nd^{3+} ($3\mu_B$) ions with Fe^{3+} ($5\mu_B$) ions [19] and graphene's non-magnetic nature and the low crystallinity are responsible for the ferrite/graphene composite's smaller value of magnetization [27, 49]. The high-frequency response of all the samples was determined using magnetic data. The response of the generated ferrites and composites will be useful in predicting their microwave device and applications. The saturation magnetization for each sample was used to determine the microwave frequency (ω_m) using the relation: $\omega_m = 8\gamma\pi^2 M_s$ where, γ = gyromagnetic fraction = 2.8 MHz/Oe. The microwave operating frequency is given in Table 3 and graphically represented in Fig. 22(d). The dimensions of the devices were found to be dependent on the material properties and frequency range used. Furthermore, the as-prepared ferrites and composite will be suitable for applications in the GHz range.

The Switching field distribution (SFD) curves [57] are plotted using the *dM/dH* and applied field (*H*) in Fig. 23. The SFD of the as-synthesized ferrites and composites is

determined by the first derivative of the demagnetization data. The cation interactions in the samples are depicted by the exhibited curves. The smooth lines in the *dM/dH* data demonstrate the cation's strong magnetic interactions at higher reverse fields. The *dM/dH* data revealed an abrupt increasing behaviour at the low field (as seen in Fig. 23). At low fields, this indicates the SFD behaviour of the synthesized ferrites. However, the NCNF/2.5wt%GNPs composite has smaller values than the NCNF/5wt%GNPs composite. The lower coercivity and higher magnetization miniaturization of devices are designed for a variety of applications including miniaturized components of high-frequency devices [58].

Conclusions

The SGAC route was used to prepare the NCF, NCNF, NCNF/2.5wt%GNPs, and NCNF/5wt%GNPs ferrites and their composites with graphene. Due to the inclusion of Nd^{3+} and GNPs, the structural analysis revealed decreased values of crystalline size and a spinel phase structure of as-prepared ferrites and composite. Raman analysis also confirmed the substitution of Nd^{3+} and GNPs. The morphological analysis revealed a reduction in the agglomeration in all the samples. The minimum energy bandgap was observed for NCNF/2.5wt%GNPs composite as compared to other prepared ferrites and composite. The resistivity decreased in the para region and increased in the ferro region with increasing the temperature. The resistivity and activation energy were maximum for the NCNF/2.5wt%GNPs composite. The TCR% plots peaks were observed at 382 K and a negative value of TCR% was found at high temperatures. Moreover, for the NCNF/2.5wt%GNPs composite, the dielectric constant has a maximum value and *ac* conductivity was a minimum. The magnetic tangent loss was maximum and dielectric tangent loss was minimum for the NCNF/2.5wt%GNPs composite. The magnetization and microwave operating frequency was 108.83 emu/g and 24.06 GHz, respectively for NCNF/2.5wt%GNPs composite. Based on these properties it was concluded that NCNF/2.5wt%GNPs composite makes them a good candidate for microwave frequency operating devices, bolometric devices, and microwave absorbing materials.

References

[1] F. Azizi, H. Jahangiri, Radar absorbing nanocomposites based multiLayered graphene platelets/epoxy, Journal of Nanostructures, 5 (2015) 345-349.
[2] A.U. Rehman, F. Afzal, M.T. Ansar, A. Sajjad, M.A. Munir, Introduction and Applications of 2D Nanomaterials, 2D Functional Nanomaterials: Synthesis, Characterization and Applications, (2021) 369-382.
[3] A. Maniadi, M. Vamvakaki, M. Suchea, I.V. Tudose, M. Popescu, C. Romanitan, C. Pachiu, O.N. Ionescu, Z. Viskadourakis, G. Kenanakis, Effect of graphene nanoplatelets on the structure, the morphology, and the dielectric behavior of low-density polyethylene nanocomposites, Materials, 13 (2020) 4776.

[4] W. Chen, Q. Liu, X. Zhu, M. Fu, One-step in situ growth of magnesium ferrite nanorods on graphene and their microwave-absorbing properties, Applied Organometallic Chemistry, 32 (2018) e4017.

[5] S. Deng, B. Wang, H. Ai, J. Han, Electromagnetic Wave Absorption Properties and Mechanism of Graphene/$Ni_{0.4}Zn_{0.6}Fe_2O_4$ Cement Composites, Journal of Materials in Civil Engineering, 34 (2022) 04022142.

[6] F.H. Mohammadabadi, S. Masoudpanah, S. Alamolhoda, H. Koohdar, Structure, magnetic, and microwave absorption properties of $(MnNiCu)_{0.9-x}Co_xZn_{0.1}Fe_2O_4$/graphene composite powders, Journal of Alloys and Compounds, 878 (2021) 160337.

[7] M.D. Stoller, S. Park, Y. Zhu, J. An, R.S. Ruoff, Graphene-based ultracapacitors, Nano letters, 8 (2008) 3498-3502.

[8] O. Akhavan, E. Ghaderi, Toxicity of graphene and graphene oxide nanowalls against bacteria, ACS nano, 4 (2010) 5731-5736.

[9] A. Rahman, M.F. Warsi, I. Shakir, M. Shahid, S. Zulfiqar, Fabrication of Ce^{3+} substituted nickel ferrite-reduced graphene oxide heterojunction with high photocatalytic activity under visible light irradiation, Journal of hazardous materials, 394 (2020) 122593.

[10] S. Qamar, S. Yasin, N. Ramzan, A. Umer, M.N. Akhtar, Structural, morphological and magnetic characterization of synthesized Co-Ce doped Ni ferrite/Graphene/BNO12 nanocomposites for practical applications, Chinese Journal of Physics, 65 (2020) 82-92.

[11] M. Bououdina, C. Manoharan, Dependence of structure/morphology on electrical/magnetic properties of hydrothermally synthesised cobalt ferrite nanoparticles, Journal of Magnetism and Magnetic Materials, 493 (2020) 165703.

[12] A. Aslam, A. Razzaq, S. Naz, N. Amin, M.I. Arshad, M. Nabi, A. Nawaz, K. Mahmood, A. Bibi, F. Iqbal, Impact of lanthanum-doping on the physical and electrical properties of cobalt ferrites, Journal of Superconductivity and Novel Magnetism, 34 (2021) 1855-1864.

[13] A. Aslam, A.U. Rehman, N. Amin, M.A. un Nabi, Q. ul ain Abdullah, N. Morley, M.I. Arshad, H.T. Ali, M. Yusuf, Z. Latif, Lanthanum doped $Zn_{0.5}Co_{0.5}La_xFe_{2-x}O_4$ spinel ferrites synthesized via co-precipitation route to evaluate structural, vibrational, electrical, optical, dielectric, and thermoelectric properties, Journal of Physics and Chemistry of Solids, 154 (2021) 110080.

[14] A.U. Rehman, N. Morley, N. Amin, M.I. Arshad, M.A. un Nabi, K. Mahmood, A. Ali, A. Aslam, A. Bibi, M.Z. Iqbal, Controllable synthesis of La^{3+} doped $Zn_{0.5}Co_{0.25}Cu_{0.25}Fe_{2-x}La_xO_4$ (x = 0.0, 0.0125, 0.025, 0.0375, 0.05) nano-ferrites by sol-gel auto-combustion route, Ceramics International, 46 (2020) 29297-29308.

[15] R. Zakir, S.S. Iqbal, A.U. Rehman, S. Nosheen, T.S. Ahmad, N. Ehsan, F. Inam, Spectral, electrical, and dielectric characterization of Ce-doped Co-Mg-Cd spinel nano-ferrites synthesized by the sol-gel auto combustion method, Ceramics International, 47 (2021) 28575-28583.

[16] M. Tsvetkov, M. Milanova, I. Ivanova, D. Neov, Z. Cherkezova-Zheleva, J. Zaharieva, M. Abrashev, Phase composition and crystal structure determination of cobalt ferrite, modified with Ce, Nd and Dy ions by X-ray and neutron diffraction, Journal of Molecular Structure, 1179 (2019) 233-241.

[17] K.K. Bharathi, J.A. Chelvane, G. Markandeyulu, Magnetoelectric properties of Gd and Nd-doped nickel ferrite, Journal of Magnetism and Magnetic Materials, 321 (2009) 3677-3680.

[18] M. Rahimi-Nasrabadi, M. Behpour, A. Sobhani-Nasab, M.R. Jeddy, Nanocrystalline Ce-doped copper ferrite: synthesis, characterization, and its photocatalyst application, Journal of Materials Science: Materials in Electronics, 27 (2016) 11691-11697.

[19] M. Kokare, N.A. Jadhav, Y. Kumar, K. Jadhav, S. Rathod, Effect of Nd^{3+} doping on structural and magnetic properties of $Ni_{0.5}Co_{0.5}Fe_2O_4$ nanocrystalline ferrites synthesized by sol-gel auto combustion method, Journal of Alloys and Compounds, 748 (2018) 1053-1061.

[20] S. Farooq, A. Saeed, M. Sharif, J. Hussain, F. Mabood, M. Iftekhar, Process optimization studies of crystal violet dye adsorption onto novel, mixed metal $Ni_{0.5}Co_{0.5}Fe_2O_4$ ferrospinel nanoparticles using factorial design, Journal of water process engineering, 16 (2017) 132-141.

[21] D. Pawar, P.P. Khirade, V. Vinayak, L. Ravangave, S. Rathod, Sol–gel auto-ignition fabrication of Gd^{3+} incorporated $Ni_{0.5}Co_{0.5}Fe_2O_4$ multifunctional spinel ferrite nanocrystals and its impact on structural, optical and magnetic properties, SN Applied Sciences, 2 (2020) 1-12.

[22] C.M. Park, Y.M. Kim, K.-H. Kim, D. Wang, C. Su, Y. Yoon, Potential utility of graphene-based nano spinel ferrites as adsorbent and photocatalyst for removing organic/inorganic contaminants from aqueous solutions: a mini review, Chemosphere, 221 (2019) 392-402.

[23] H. Yang, T. Ye, Y. Lin, J. Zhu, F. Wang, Microwave absorbing properties of the ferrite composites based on graphene, Journal of Alloys and Compounds, 683 (2016) 567-574.

[24] P. Yin, Y. Deng, L. Zhang, W. Wu, J. Wang, X. Feng, X. Sun, H. Li, Y. Tao, One-step hydrothermal synthesis and enhanced microwave absorption properties of $Ni_{0.5}Co_{0.5}Fe_2O_4$/graphene composites in low frequency band, Ceramics International, 44 (2018) 20896-20905.

[25] S. Zhang, Q. Jiao, J. Hu, J. Li, Y. Zhao, H. Li, Q. Wu, Vapor diffusion synthesis of rugby-shaped $CoFe_2O_4$/graphene composites as absorbing materials, Journal of Alloys and Compounds, 630 (2015) 195-201.

[26] K.L. Routray, S. Saha, D. Behera, Nanosized $CoFe_2O_4$-graphene nanoplatelets with massive dielectric enhancement for high frequency device application, Materials Science and Engineering: B, 257 (2020) 114548.

[27] S. Qamar, M.N. Akhtar, W. Aleem, Z. ur Rehman, A.H. Khan, A. Ahmad, K.M. Batoo, M. Aamir, Graphene anchored Ce doped spinel ferrites for practical and technological applications, Ceramics International, 46 (2020) 7081-7088.

[28] M.N. Akhtar, M. Yousaf, Y. Lu, M.Z. Mahmoud, J. Iqbal, M.A. Khan, M.U. Khallidoon, S. Ullah, M. Hussien, Magnetic, structural, optical band alignment and conductive analysis of graphene-based REs (Yb, Gd, and Sm) doped $NiFe_2O_4$ nanocomposites for emerging technological applications, Synthetic Metals, 284 (2022) 116994.

[29] M. Nawaz, M. Islam, M.A. Nazir, I. Bano, I. Gul, M. Ajmal, Transport properties in spinel ferrite/graphene oxide nanocomposites for electromagnetic shielding, Ceramics International, 47 (2021) 25505-25513.

[30] T. Aissou, N. Braidy, J. Veilleux, A new one-step deposition approach of graphene nanoflakes coating using a radio frequency plasma: Synthesis, characterization and tribological behaviour, Tribology International, 167 (2022) 107406.

[31] P. Liu, Y. Huang, X. Zhang, Synthesis and excellent microwave absorption properties of graphene/polypyrrole composites with Fe_3O_4 particles prepared via a co-precipitation method, Materials Letters, 129 (2014) 35-38.

[32] B. Wei, L. Wang, Q. Miao, Y. Yuan, P. Dong, R. Vajtai, W. Fei, Fabrication of manganese oxide/three-dimensional reduced graphene oxide composites as the supercapacitors by a reverse microemulsion method, Carbon, 85 (2015) 249-260.

[33] J. Zhang, Z. Chen, J. Zhao, Z. Jiang, Microstructure and mechanical properties of aluminium-graphene composite powders produced by mechanical milling, Mechanics of Advanced Materials and Modern Processes, 4 (2018) 1-9.

[34] M. Rahimi-Nasrabadi, M. Rostami, F. Ahmadi, A.F. Shojaie, M.D. Rafiee, Synthesis and characterization of $ZnFe_{2-x}Yb_xO_4$–graphene nanocomposites by sol–gel method, Journal of Materials Science: Materials in Electronics, 27 (2016) 11940-11945.

[35] B. Saravanakumar, R. Mohan, S.J. Kim, Facile synthesis of graphene/ZnO nanocomposites by low temperature hydrothermal method, Materials Research Bulletin, 48 (2013) 878-883.

[36] A. Aslam, A.U. Rehman, N. Amin, M. Amami, M. Nabi, H. Alrobei, M. Asghar, N. Morley, M. Akhtar, M.I. Arshad, Sol–Gel auto-combustion preparation of $M^{2+} = Mg^{2+}$, Mn^{2+}, Cd^{2+} substituted $M_{0.25}Ni_{0.15}Cu_{0.25}Co_{0.35}Fe_2O_4$ ferrites and their characterizations, Journal of Superconductivity and Novel Magnetism, 35 (2022) 473-483.

[37] P. Samoila, L. Sacarescu, A. Borhan, D. Timpu, M. Grigoras, N. Lupu, M. Zaltariov, V. Harabagiu, Magnetic properties of nanosized Gd doped Ni–Mn–Cr ferrites prepared using the sol–gel autocombustion technique, Journal of Magnetism and Magnetic Materials, 378 (2015) 92-97.

[38] N. Amin, A. Razaq, A.U. Rehman, K. Hussain, M. Nabi, N. Morley, M. Amami, A. Bibi, M.I. Arshad, K. Mahmood, Transport properties of Ce-doped Cd ferrites $CdFe_{2-x}Ce_xO_4$, Journal of Superconductivity and Novel Magnetism, 34 (2021) 2945-2955.

[39] B. Bashir, W. Shaheen, M. Asghar, M.F. Warsi, M.A. Khan, S. Haider, I. Shakir, M. Shahid, Copper doped manganese ferrites nanoparticles anchored on graphene nano-sheets for high performance energy storage applications, Journal of Alloys and Compounds, 695 (2017) 881-887.

[40] P. Galinetto, B. Albini, M. Bini, M.C. Mozzati, Raman spectroscopy in zinc ferrites nanoparticles, Raman Spectrosc, 223 (2018).

[41] S.B. Somvanshi, S.A. Jadhav, M.V. Khedkar, P.B. Kharat, S. More, K. Jadhav, Structural, thermal, spectral, optical and surface analysis of rare earth metal ion (Gd^{3+}) doped mixed Zn–Mg nano-spinel ferrites, Ceramics International, 46 (2020) 13170-13179.

[42] G. Abbas, A.U. Rehman, W. Gull, M. Afzaal, N. Amin, L. Ben Farhat, M. Amami, N.A. Morley, M. Akhtar, M.I. Arshad, Impact of Co^{2+} on the spectral, optoelectrical, and dielectric properties of $Mg_{0.25}Ni_{0.25}Cu_{0.5-x}Co_xFe_{1.97}La_{0.03}O_4$ ferrites prepared via sol–gel auto-combustion route, Journal of Sol-Gel Science and Technology, (2022) 1-15.

[43] M.I.U. Haq, M. Asghar, M.A.U. Nabi, N. Amin, S. Tahir, M.I. Arshad, Influence of Ce^{3+} and La^{3+} Substitution on Structural & Optical Parameters and Electrical Behavior on Mg-Zn Ferrites Synthesized via Co-precipitation method, Journal of Superconductivity and Novel Magnetism, 35 (2022) 719-732.

[44] K. Hussain, N. Amin, M.I. Arshad, Evaluation of structural, optical, dielectric, electrical, and magnetic properties of Ce^{3+} doped $Cu_{0.5}Cd_{0.25}Co_{0.25}Fe_{2-x}O_4$ spinel nano-ferrites, Ceramics International, 47 (2021) 3401-3410.

[45] A.S. Fawzi, A. Sheikh, V. Mathe, Structural, dielectric properties and AC conductivity of $Ni_{(1-x)}Zn_xFe_2O_4$ spinel ferrites, Journal of Alloys and Compounds, 502 (2010) 231-237.

[46] M.I. Arshad, M. Hasan, A.U. Rehman, M. Akhtar, N. Amin, K. Mahmood, A. Ali, T. Trakoolwilaiwan, N.T.K. Thanh, Structural, optical, electrical, dielectric, molecular vibrational and magnetic properties of La^{3+} doped Mg–Cd–Cu ferrites prepared by Co-precipitation technique, Ceramics International, 48 (2022) 14246-14260.

[47] A.U. Rehman, N. Amin, M.B. Tahir, M.A. un Nabi, N. Morley, M. Alzaid, M. Amami, M. Akhtar, M.I. Arshad, Evaluation of spectral, optoelectrical, dielectric, magnetic, and morphological properties of RE^{3+} (La^{3+}, and Ce^{3+}) and Co^{2+} co-doped $Zn_{0.75}Cu_{0.25}Fe_2O_4$ ferrites, Materials Chemistry and Physics, 275 (2022) 125301.

[48] A. Dimiev, W. Lu, K. Zeller, B. Crowgey, L.C. Kempel, J.M. Tour, Low-loss, high-permittivity composites made from graphene nanoribbons, ACS applied materials and interfaces, 3 (2011) 4657-4661.

[49] F.H. Mohammadabadi, S. Masoudpanah, S. Alamolhoda, H. Koohdar, Electromagnetic microwave absorption properties of high entropy spinel ferrite $((MnNiCuZn)_{1-x}Co_xFe_2O_4)$/graphene nanocomposites, Journal of Materials Research and Technology, 14 (2021) 1099-1111.

[50] M.A. Darwish, A.V. Trukhanov, O.S. Senatov, A.T. Morchenko, S.A. Saafan, K.A. Astapovich, S.V. Trukhanov, E.L. Trukhanova, A.A. Pilyushkin, A.S.B. Sombra, Investigation of AC-measurements of epoxy/ferrite composites, Nanomaterials, 10 (2020) 492.

[51] A. Gholizadeh, M. Beyranvand, Investigation on the structural, magnetic, dielectric and impedance analysis of $Mg_{0.3-x}Ba_xCu_{0.2}Zn_{0.5}Fe_2O_4$ nanoparticles, Physica B: Condensed Matter Physics, 584 (2020) 412079.

[52] M.M. Hossen, S. Nasrin, M.B. Hossen, Effect of Mn^{2+} doping on structural, magnetic and electrical properties of $Ni_{0.5-x}Mn_xCu_{0.2}Cd_{0.3}Fe_2O_4$ nano ferrites prepared by sol-gel auto combustion method for high-frequency applications, Physica B: Condensed Matter, 599 (2020) 412456.

[53] M.S. Kumar, G. Shankarmurthy, E. Melagiriyappa, K. Nagaraja, H. Jayanna, M. Telenkov, Induced effects of Zn^{+2} on the transport and complex impedance properties of Gadolinium substituted nickel-zinc nano ferrites, Journal of magnetism and Magnetic materials, 478 (2019) 12-19.

[54] F. Alam, M. Rahman, M. Khan, A.A. Hossain, Magnetic Hysteresis and Complex Initial Permeability of Cr^{3+} Substituted Mn-Zn Ferrites, Journal of Modern Physics, 2014 (2014).

[55] G. Gan, D. Zhang, J. Li, G. Wang, X. Huang, Y. Yang, Y. Rao, F. Xu, X. Wang, H. Zhang, Equivalent permeability and permittivity of Sm substituted Mg–Cd ferrites for high-frequency applications, Journal of Alloys and Compounds, 819 (2020) 153059.

[56] J. Li, W. Lu, J. Suhr, H. Chen, J.Q. Xiao, T.-W. Chou, Superb electromagnetic wave-absorbing composites based on large-scale graphene and carbon nanotube films, Scientific reports, 7 (2017) 1-10.

[57] M.N. Akhtar, M.S. Nazir, M.A. Khan, S. Ullah, M.A. Assiri, Preparations and characterizations of Ca doped Ni–Mg–Mn nanocrystalline ferrites for switching field high-frequency applications, Ceramics International, 48 (2022) 3833-3840.

[58] M.N. Akhtar, K. Ali, A. Umer, T. Ahmad, M.A. Khan, Structural elucidation, and morphological and magnetic behavior evaluations, of low-temperature sintered, Ce-doped, nanostructured garnet ferrites, Materials Research Bulletin, 101 (2018) 48-55.

Tables

Table 1: Structural parameters of as-prepared composites

Samples	d (Å)	a (Å)	V (Å³)	β (degree)	D (nm)	$\delta \times 10^{-4}$ (nm⁻²)	ε (%)
NCF	2.517	8.348	581.88	0.26	33.49	8.91	0.353
NCNF	2.515	8.341	580.45	0.25	34.83	8.24	0.339
NCNF/2.5wt% GNPs	2.518	8.353	582.82	0.23	37.85	6.97	0.312
NCNF/5wt% GNPs	2.531	8.396	591.95	0.22	39.55	6.38	0.301

Table 2 Raman modes for all the samples

Samples	Raman shift (cm⁻¹)					D	G
	$T_{2g}(1)$	E_g	$T_{2g}(2)$	$T_{2g}(3)$	A_{1g}		
	Tetrahedral (A) Site	Octahedral (B) site			Tetrahedral (A) Site		
NCF	316.72	375.08	486.38	608.16	689.65	----	----
NCNF	316.56	383.96	463.29	556.04	692.03	----	----
NCNF/2.5wt% GNPs	286.99	402.61	487.40	607.06	695.89	1315.11	1596.28
NCNF/5wt% GNPs	313.76	389.03	461.71	556.77	685.61	1316.56	1590.41

Table 3 Magnetic parameters for all the as-prepared samples

Samples	H_C (Oe)	M_r (emu/g)	M_s (emu/g)	SQ	K (erg/cm³)	ω_m (GHz)	μ_i
NCF	495.46	62.02	117.73	0.5268	60760.94	26.02	7.63
NCNF	122.71	37.58	114.05	0.3295	14578.20	25.21	31.07
NCNF/2.5wt%GNPs	250.61	47.05	108.83	0.4323	28410.29	24.06	15.77
NCNF/5wt% GNPs	397.41	39.55	93.97	0.4208	38900.64	20.77	8.97
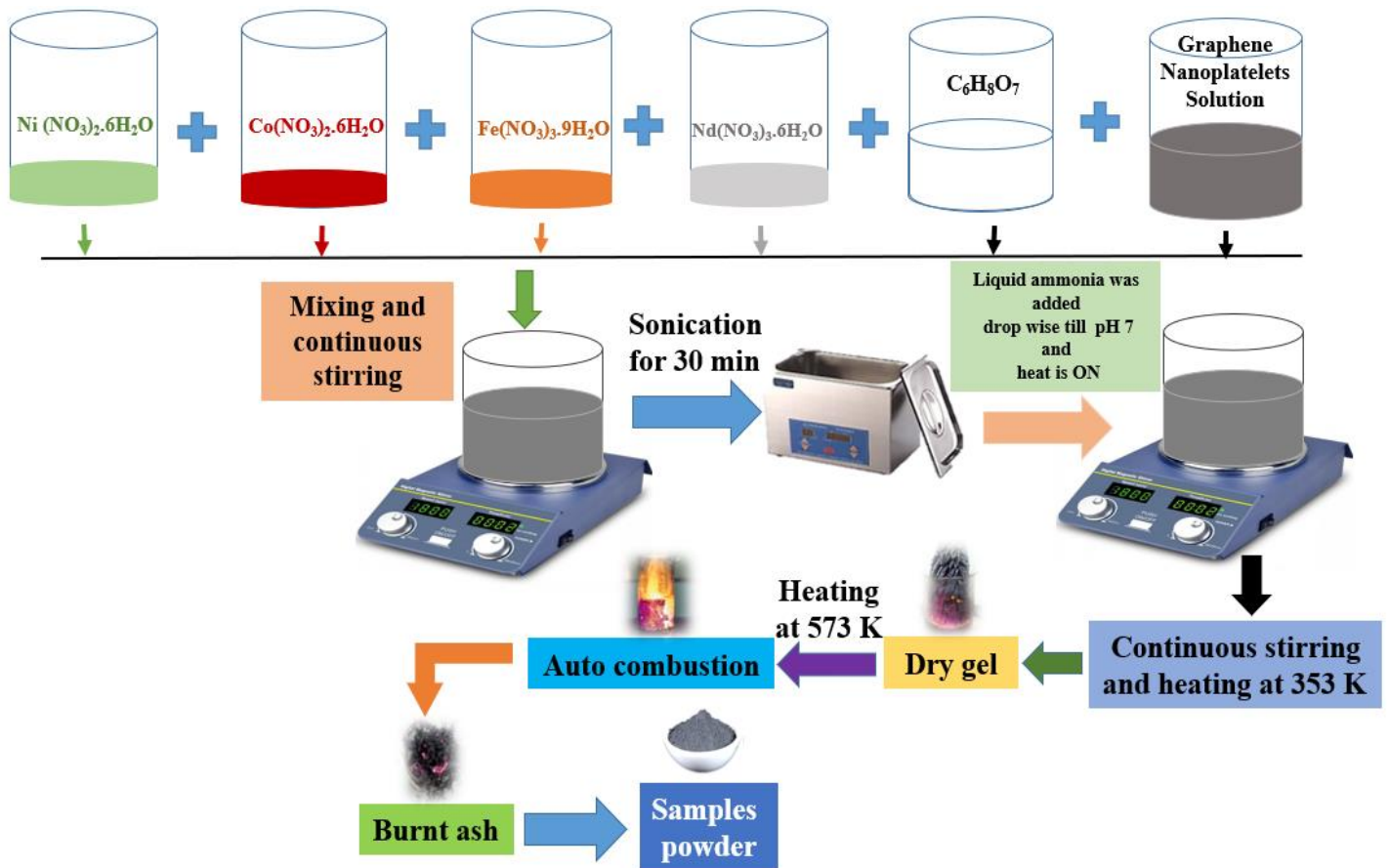
Fig. 1 Graphic representation of the synthesis of all the samples
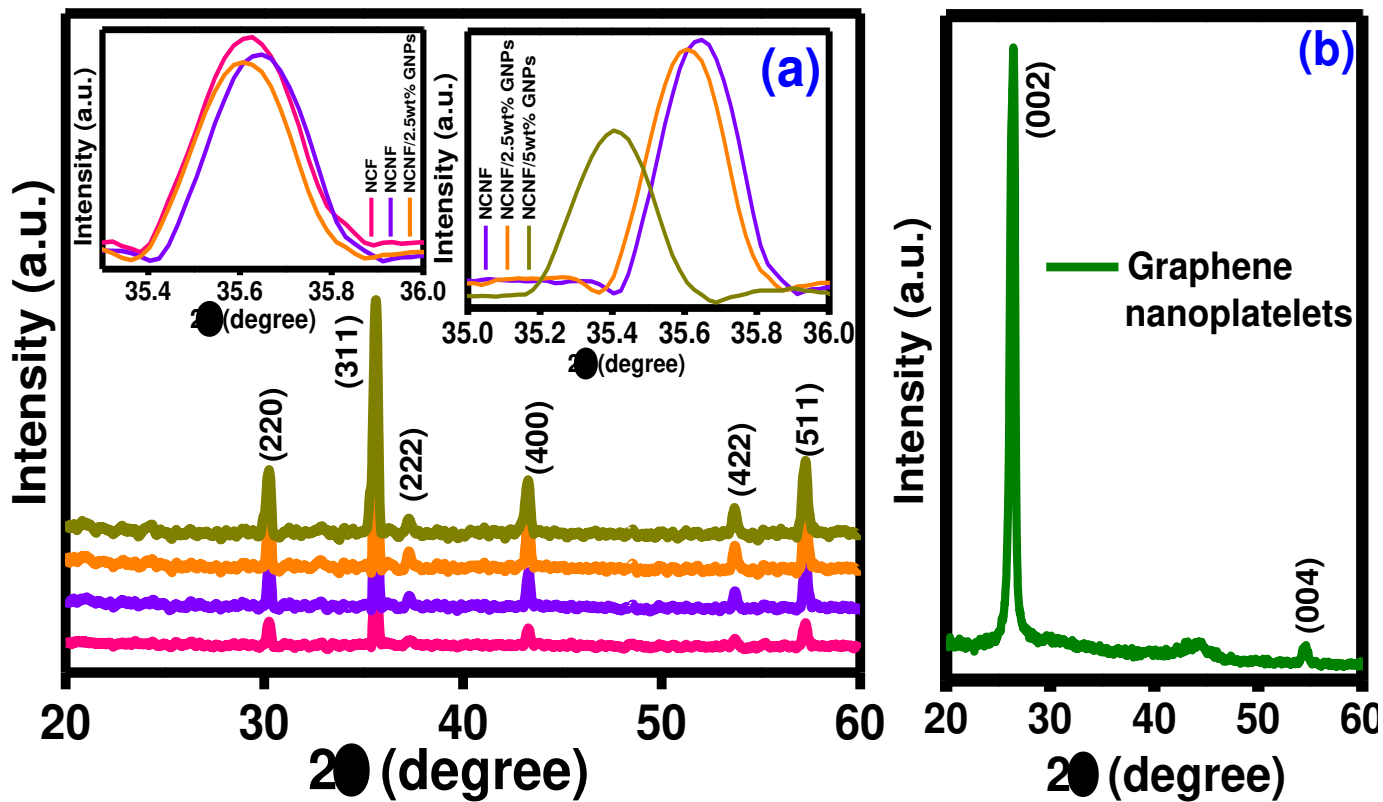
Fig. 2 (a) XRD spectra for NCF, NCNF, NCNF/2.5wt%GNPs, and NCNF/5wt%GNPs composites **(b)** Peak shift in (311) plane in all the as-prepared samples **(c)** XRD spectra of graphene nanoplatelets
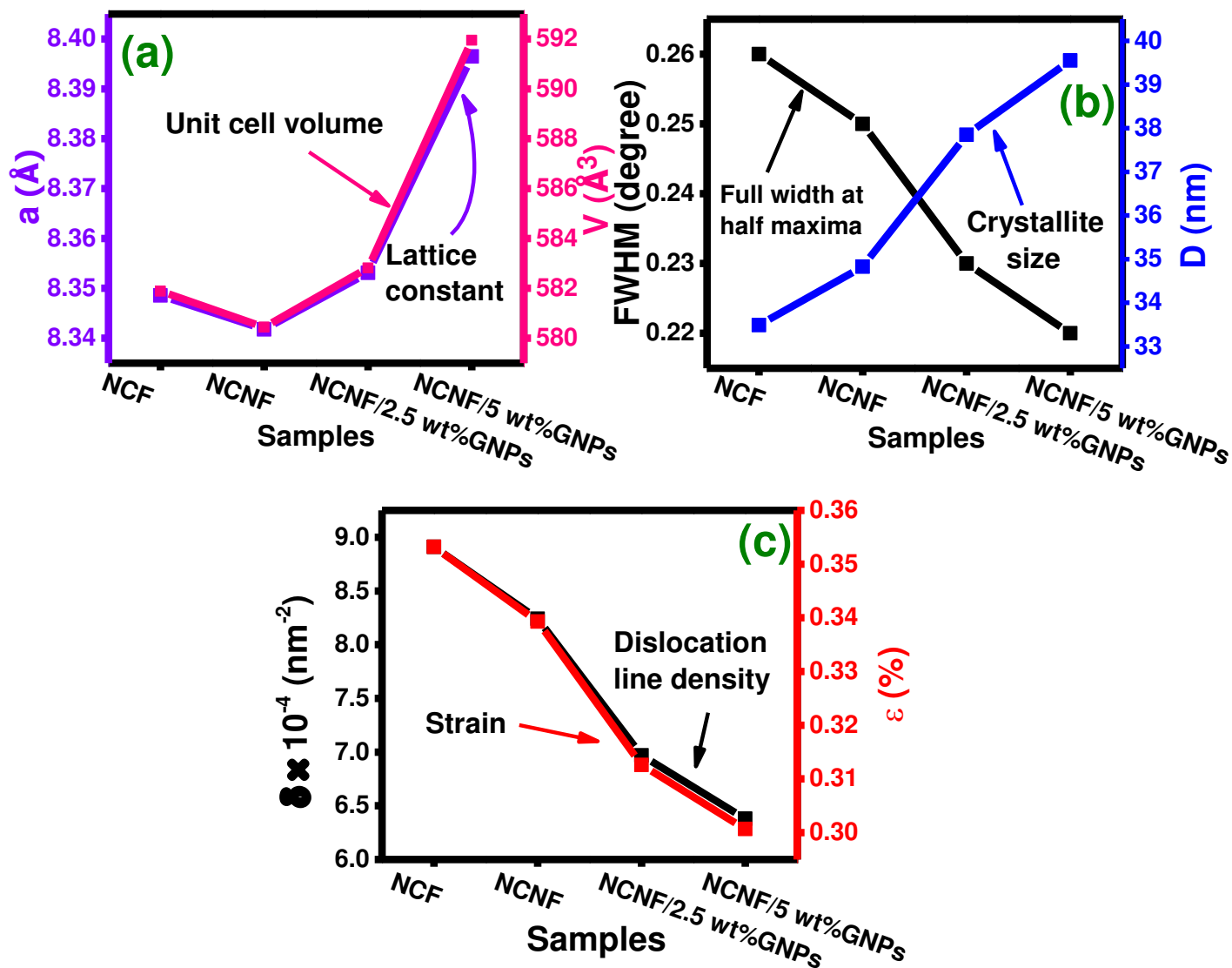
Fig. 3 Samples *versus* (**a**) lattice constant and unit cell volume (**b**) full width at half maxima and crystallite size (**c**) dislocation line density and strain for all the samples
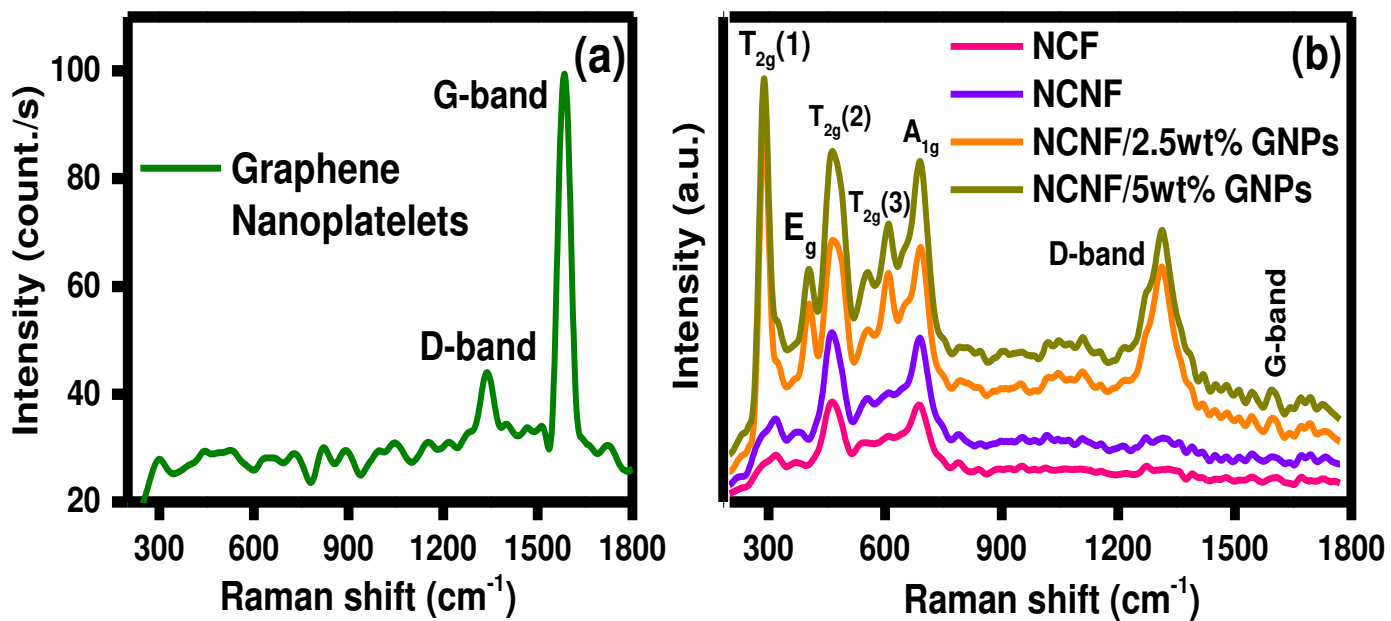
Fig. 4 (a) Raman spectra of graphene nanoplatelets **(b)** Raman spectra for NCF, NCNF, NCNF/2.5wt%GNPs, and NCNF/5wt%GNPs composites
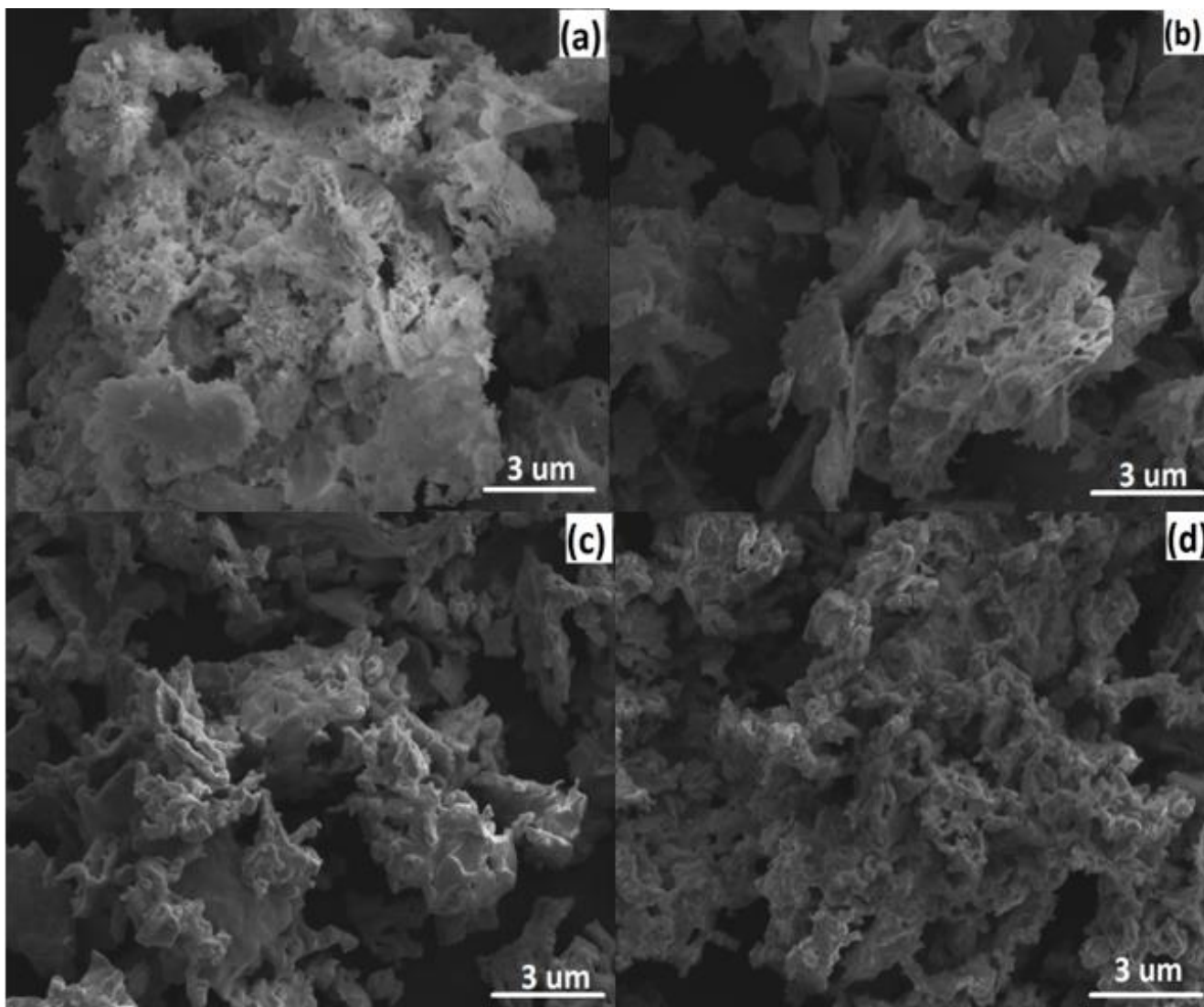
Fig. 5(a) Micrograph for NCF sample **(b)** Micrograph for NCNF sample **(c)** Micrograph for NCNF/2.5wt%GNPs composite **(d)** Micrograph for NCNF/5wt%GNPs composite
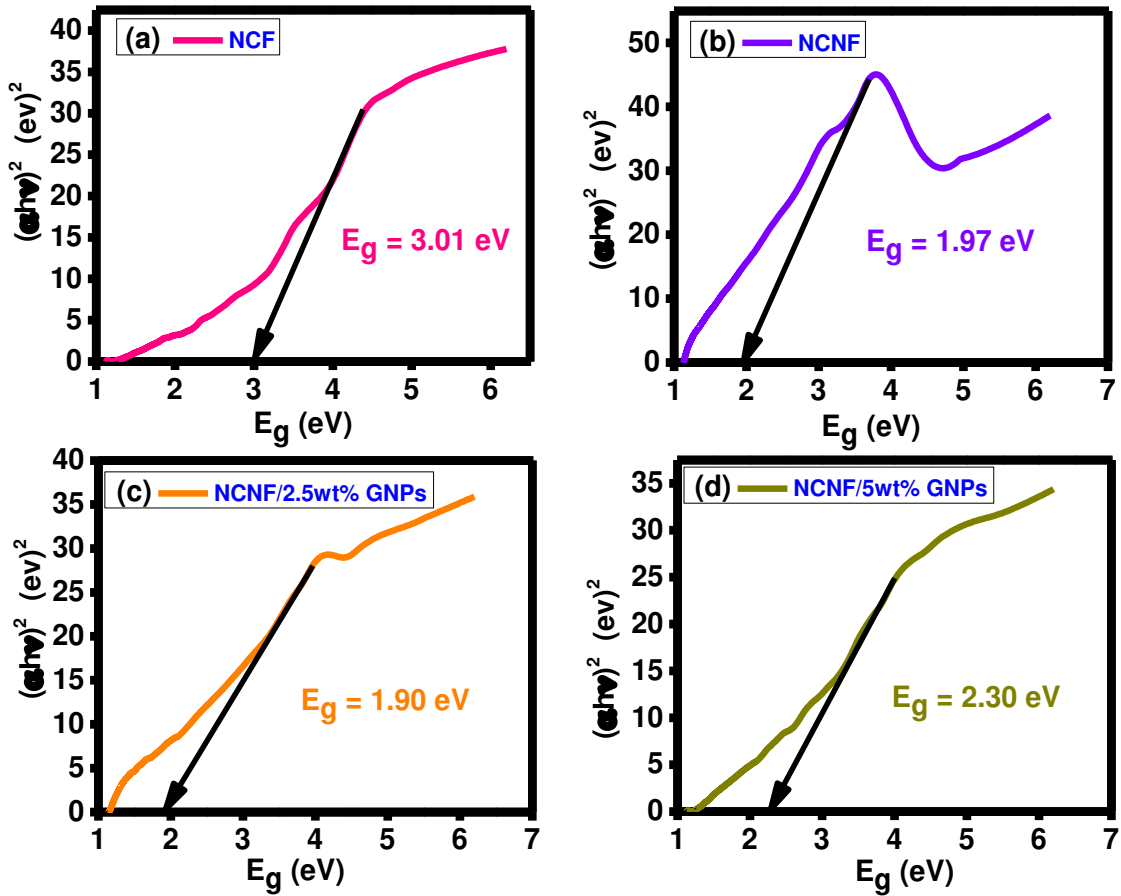
Fig. 6(a) Tauc plot for NCF sample **(b)** Tauc plot for NCNF sample **(c)** Tauc plot for NCNF/2.5wt%GNPs composite **(d)** Tauc plot for NCNF/5wt%GNPs composite
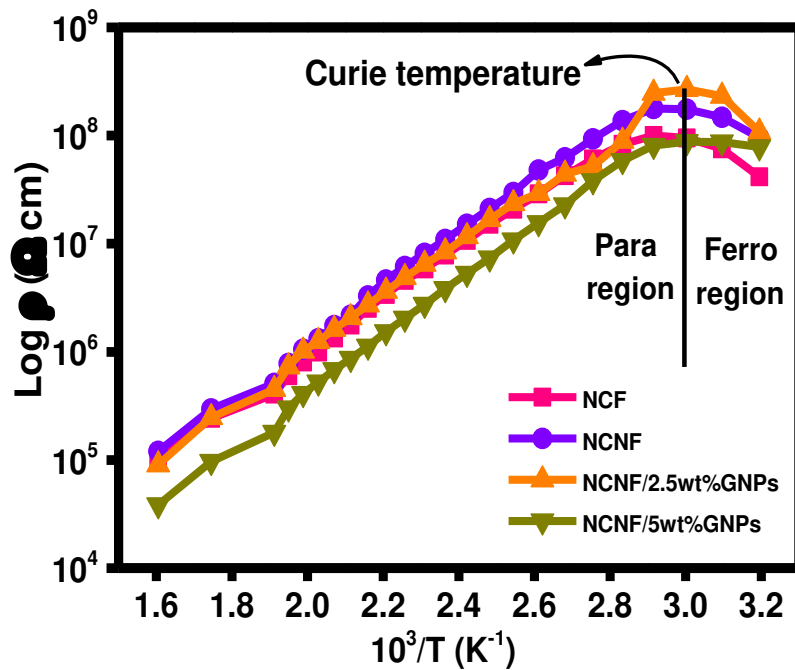
Fig. 7 Plots of 10^3/T *versus* the log of resistivity of all the samples
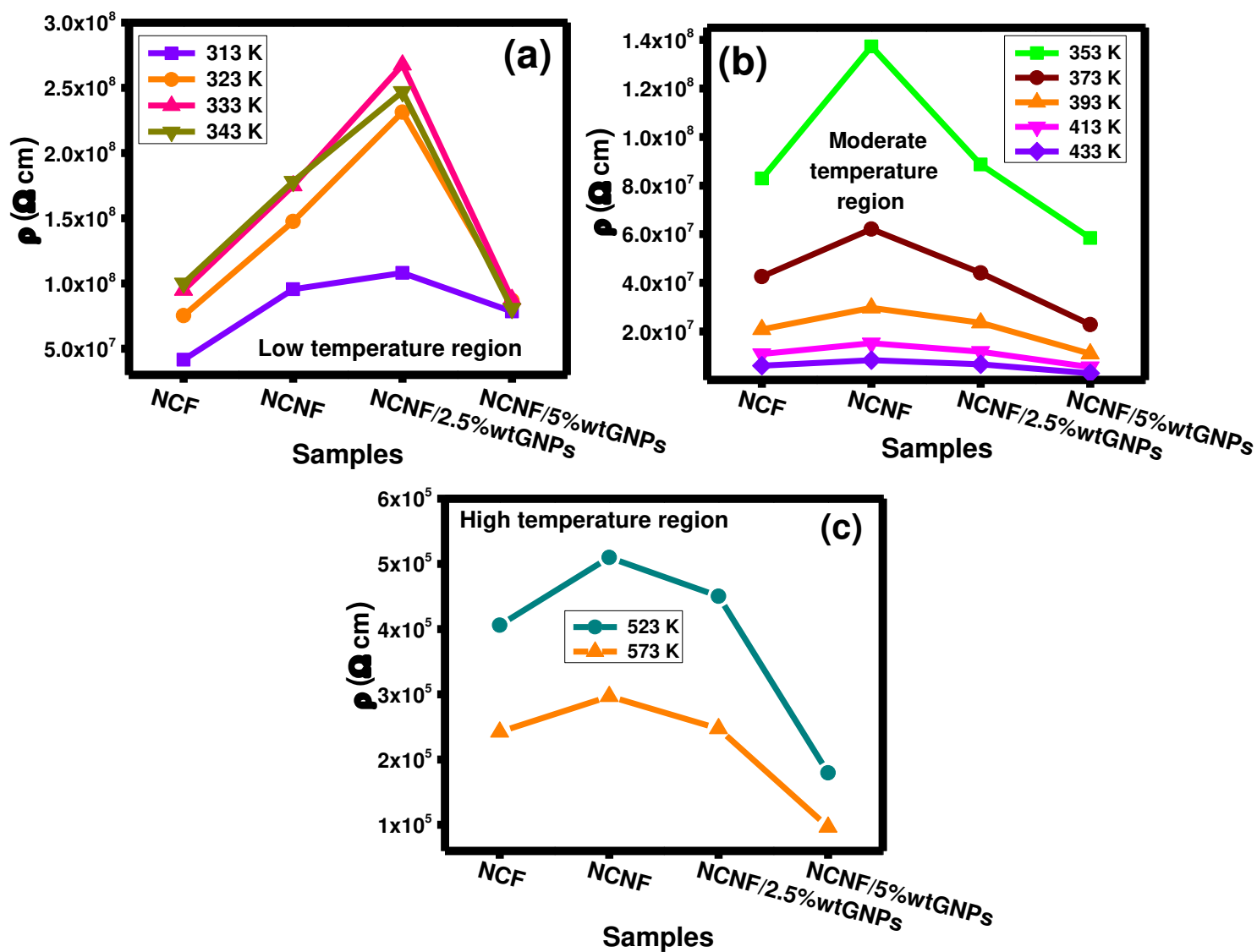
Fig. 8 Samples *versus* (**a**) resistivity at low temperature (**b**) resistivity at moderate temperature (**c**) resistivity at high temperature
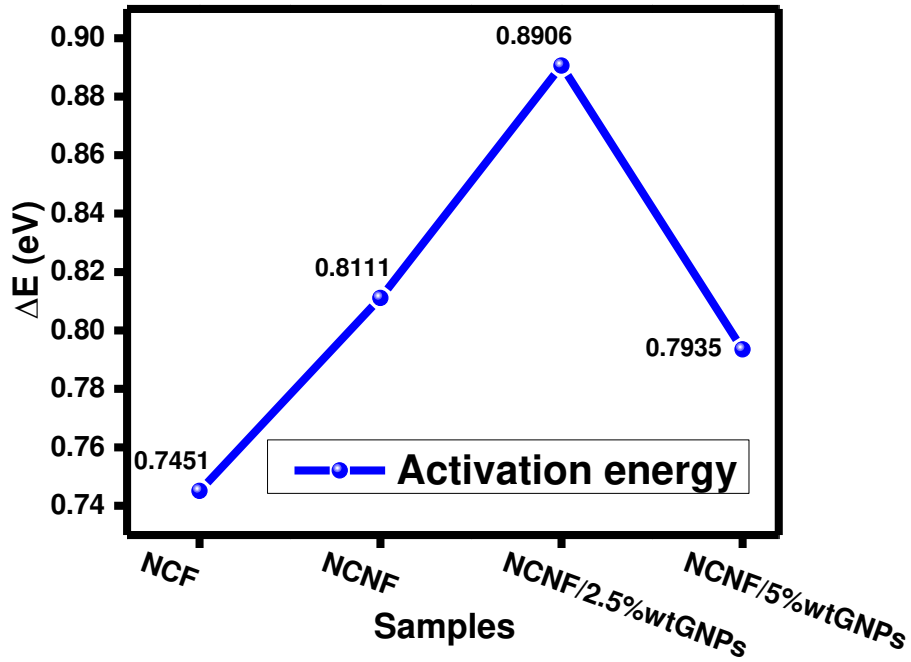
Fig. 9 Samples *versus* activation energy for all the samples
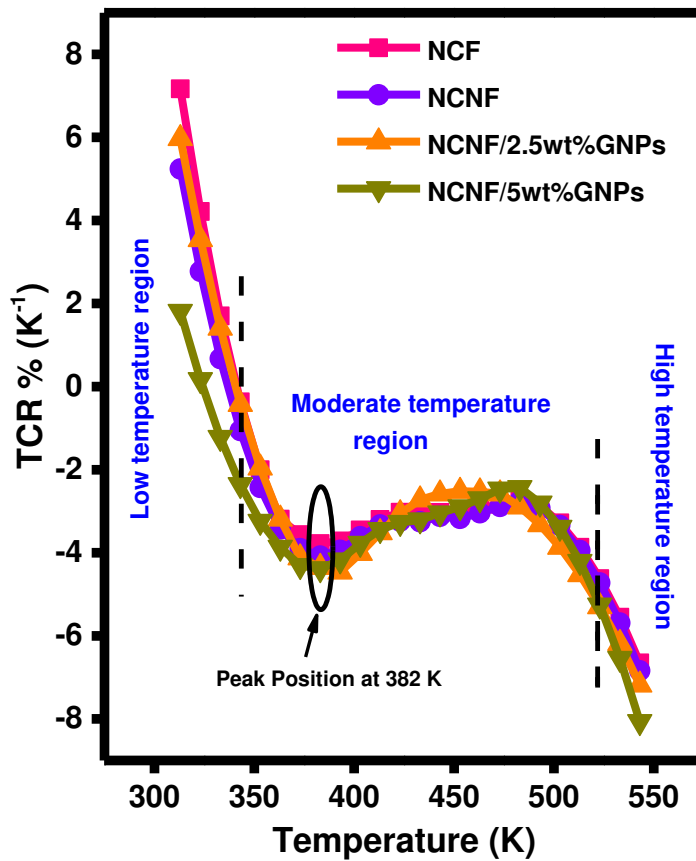
Fig. 10 Temperature *versus* temperature coefficient of resistance percentage for all the samples
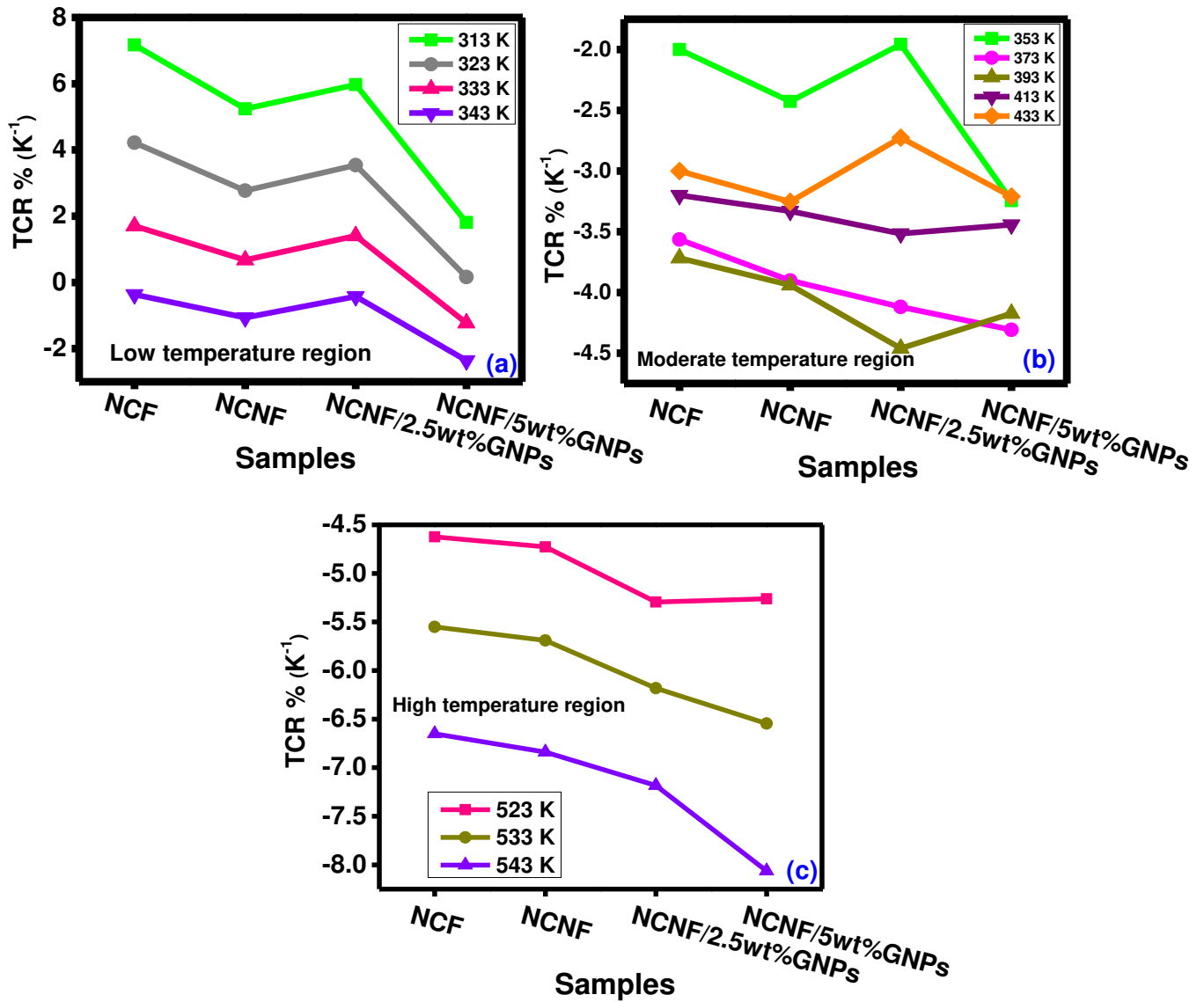
Fig. 11 Samples *versus* (**a**) TCR% at low temperature (**b**) TCR% at moderate temperature and (**c**) TCR% at high temperature
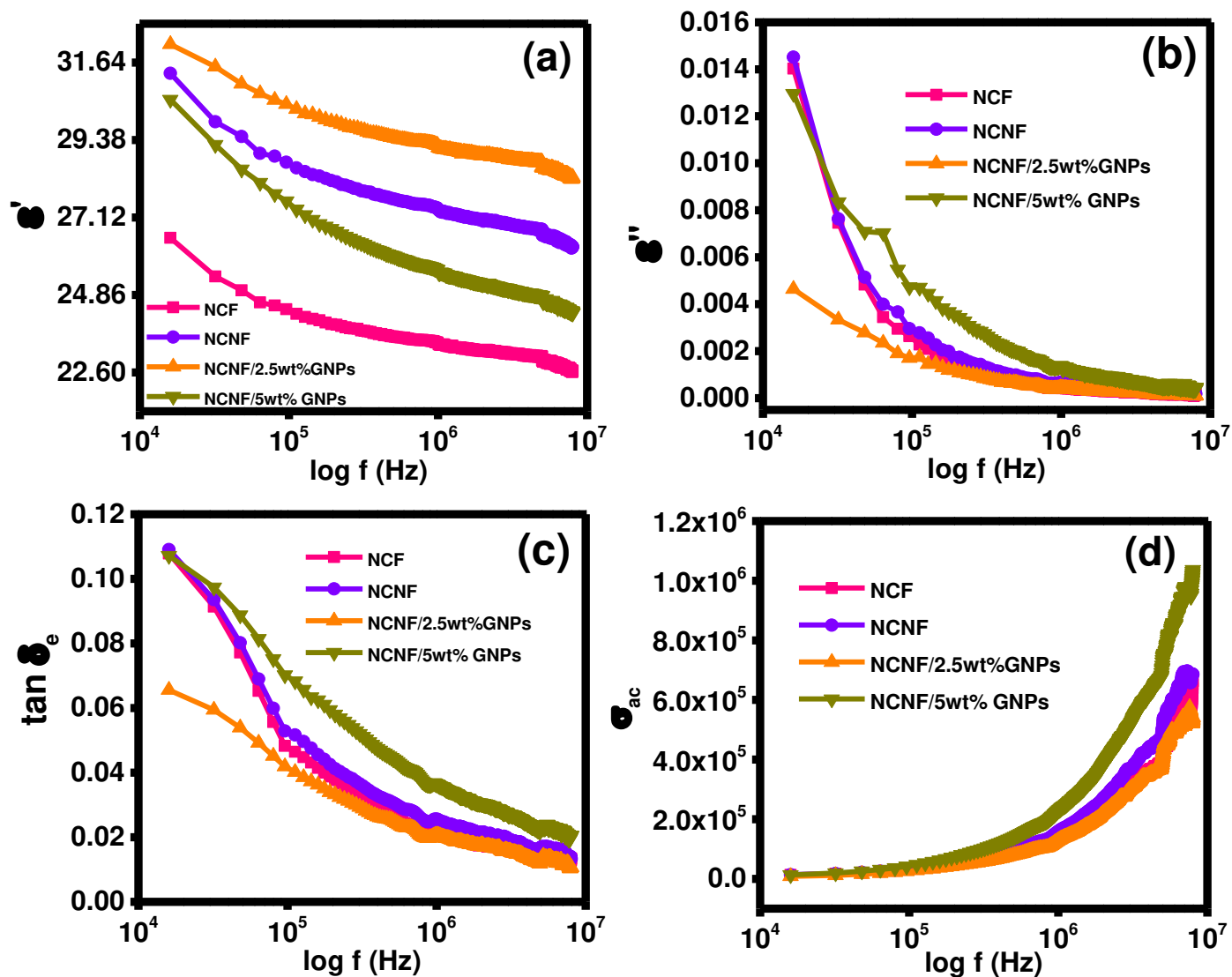
Fig. 12 log of frequency versus **(a)** dielectric constant **(b)** dielectric loss **(c)** tangent loss **(d)** ac conductivity for all the samples
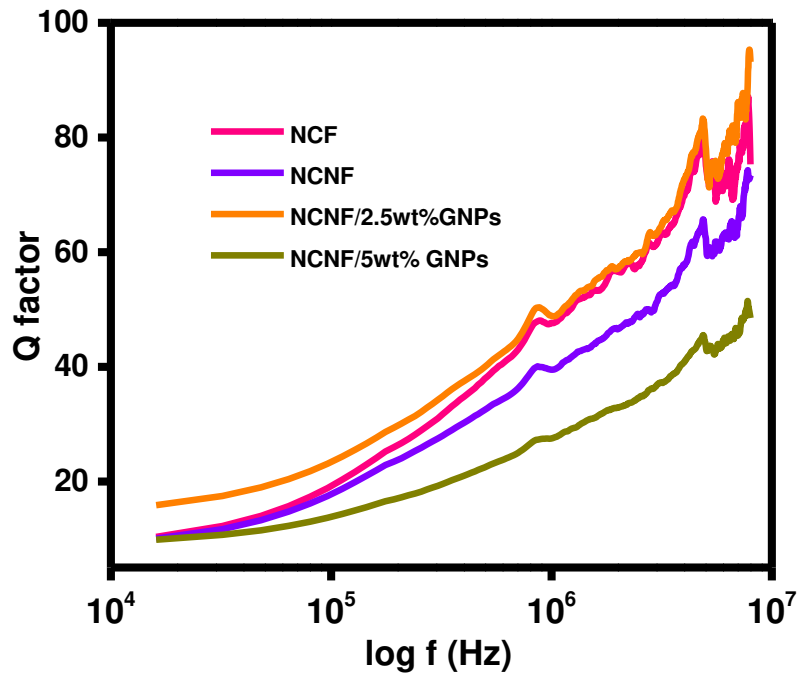
Fig. 13 log of frequency *versus Q* factors for all the samples
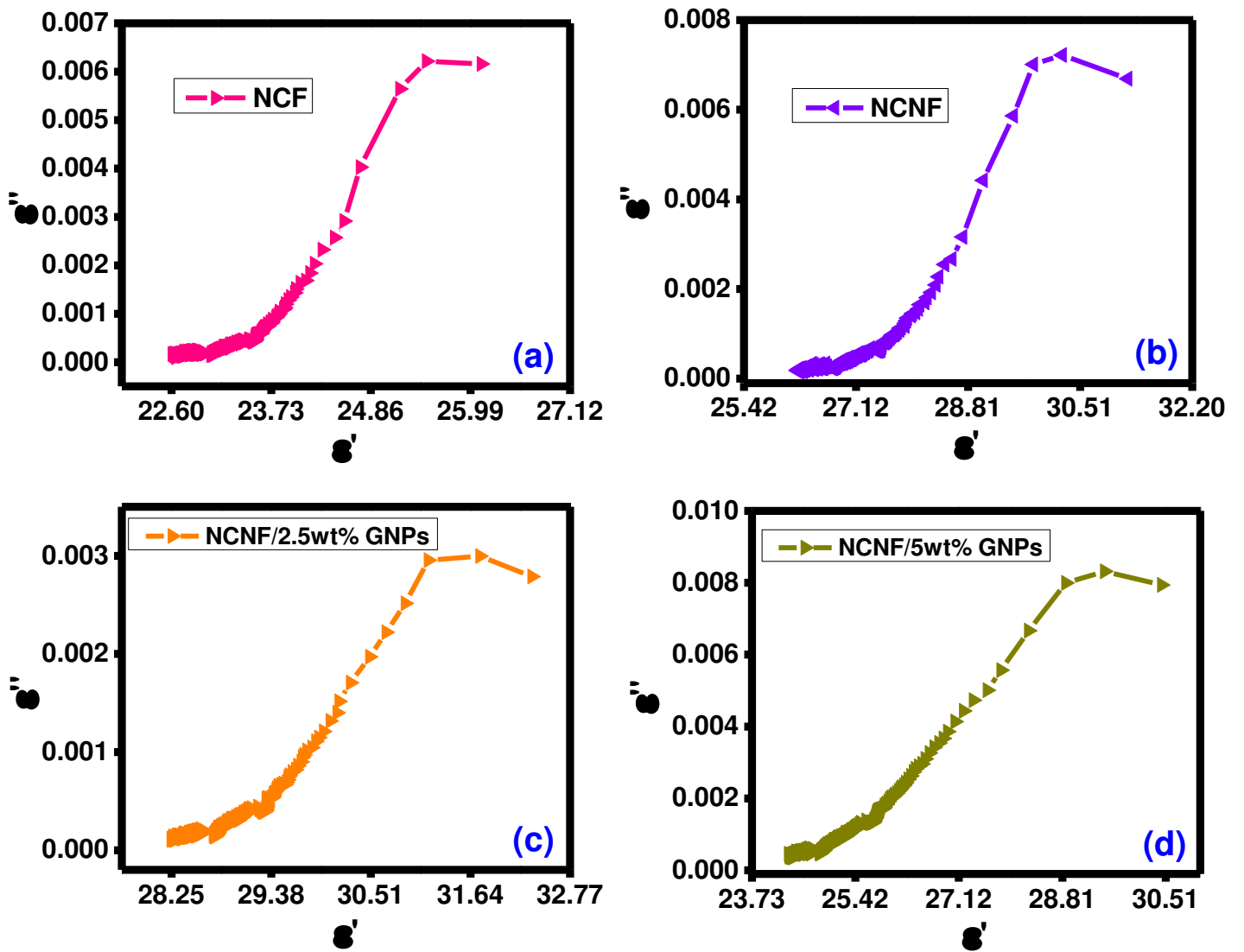
Fig. 14(a) Cole-Cole plot for NCF sample **(b)** Cole-Cole plot for NCNF sample **(c)** Cole-Cole plot for NCNF/2.5wt%GNPs composite **(d)** Cole-Cole plot for NCNF/5wt%GNPs composite
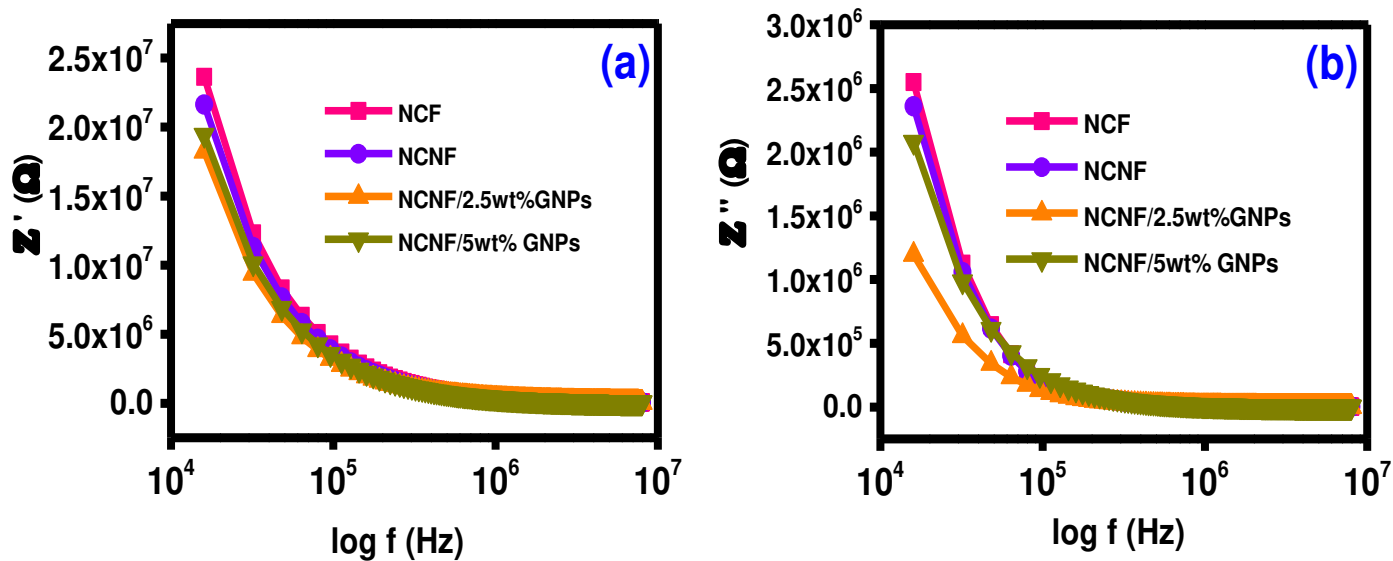
Fig. 15 log of frequency versus **(a)** real part of impedance **(b)** imaginary part of impedance for NCF, NCNF, NCNF/2.5wt%GNPs, and NCNF/5wt%GNPs composites
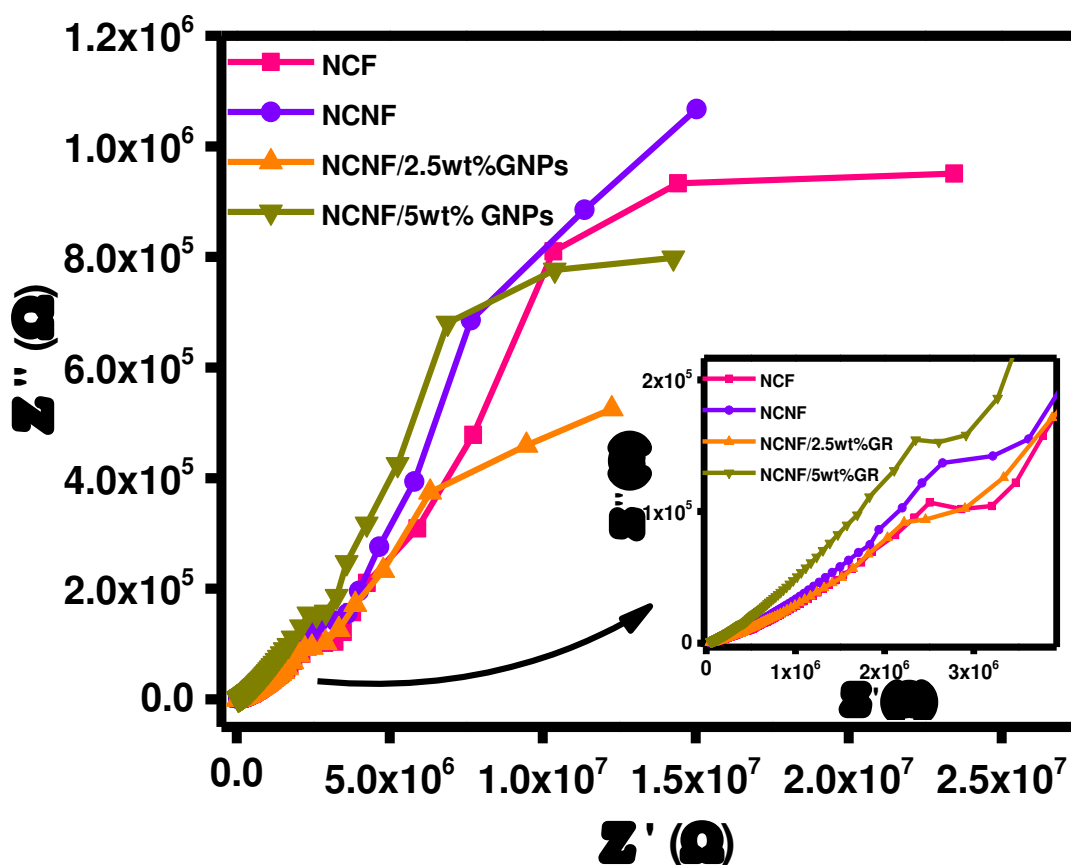
Fig. 16 Nyquist plots for NCF, NCNF, NCNF/2.5wt%GNPs, and NCNF/5wt%GNPs composites
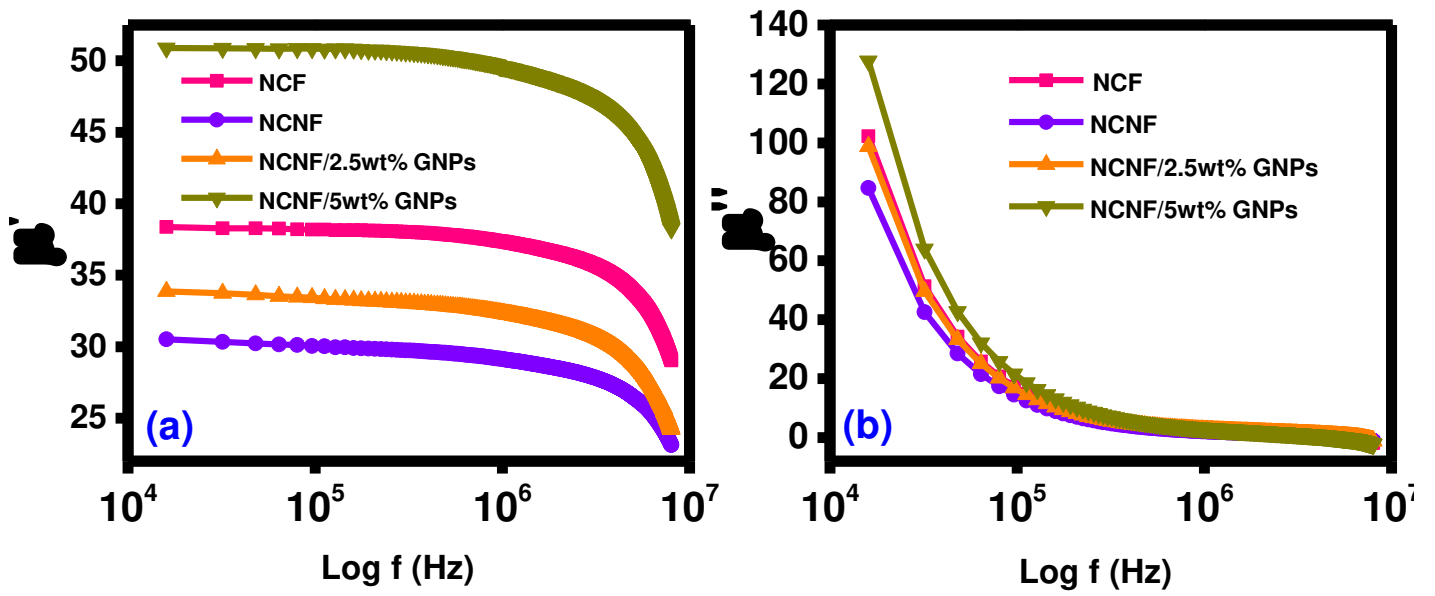
Fig. 17 log of frequency *versus* (**a**) real part of complex initial permeability (**b**) imaginary part of complex initial permeability for all the samples
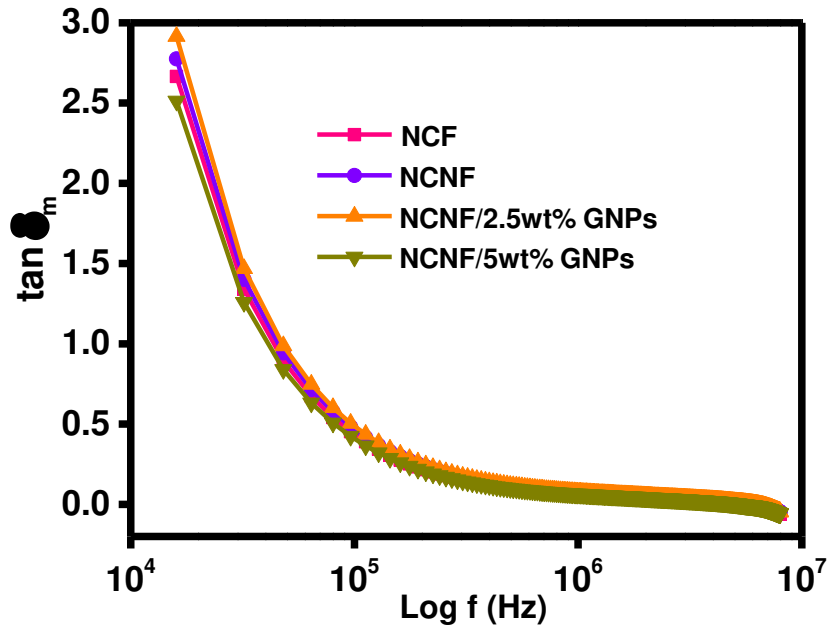
Fig. 18 Magnetic tangent loss for all the samples
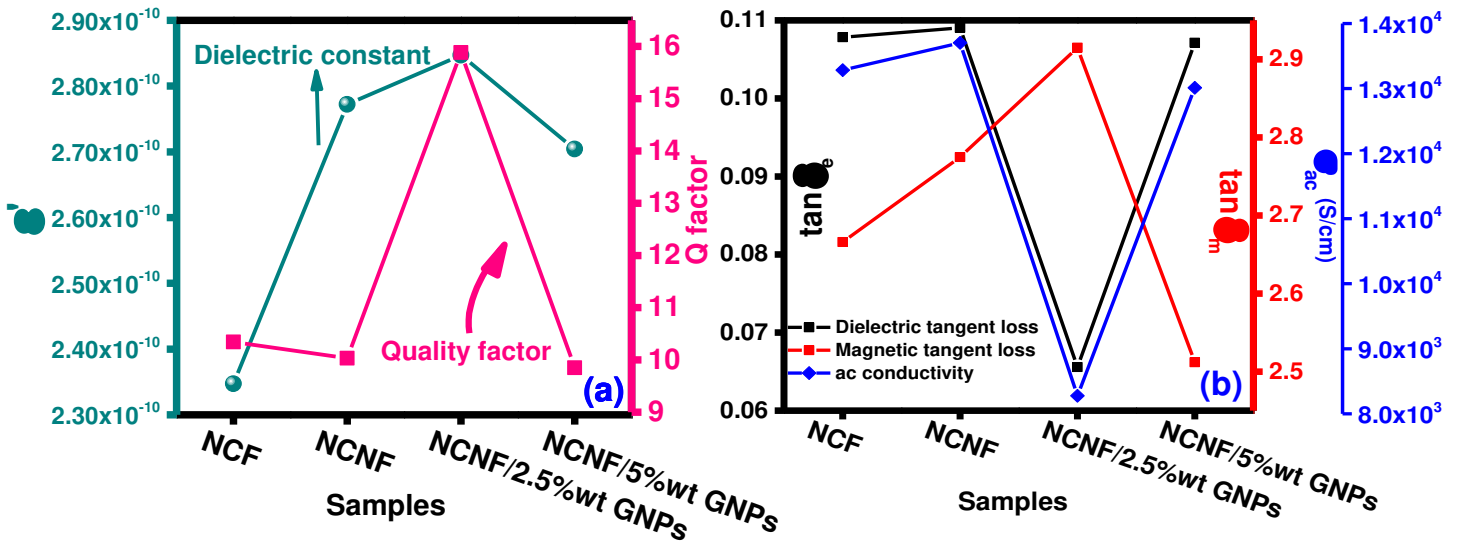
Fig. 19 Samples *versus* (**a**) dielectric constant, and quality factor (**b**) *ac* conductivity, dielectric, and magnetic tangent losses at 15 kHz
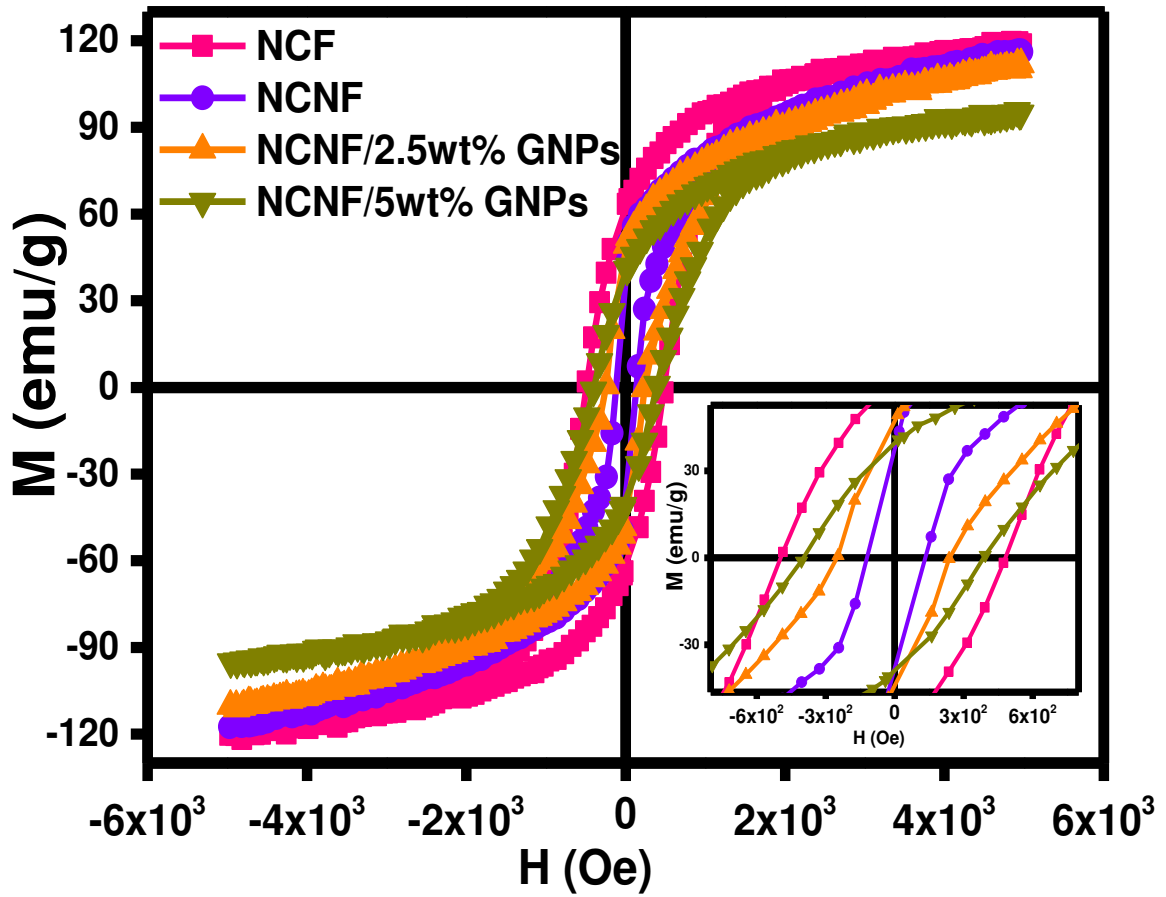
Fig. 20 M-H loop for as-prepared ferrites and composites
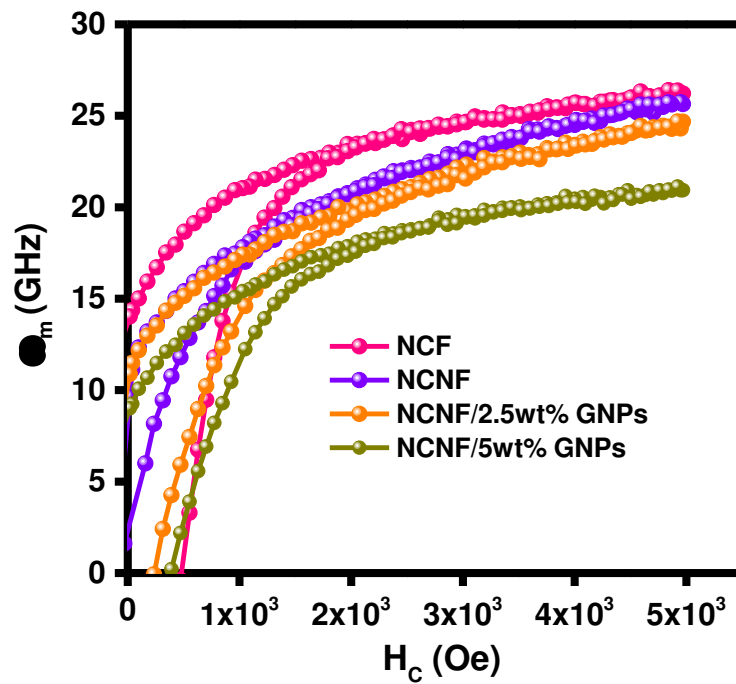

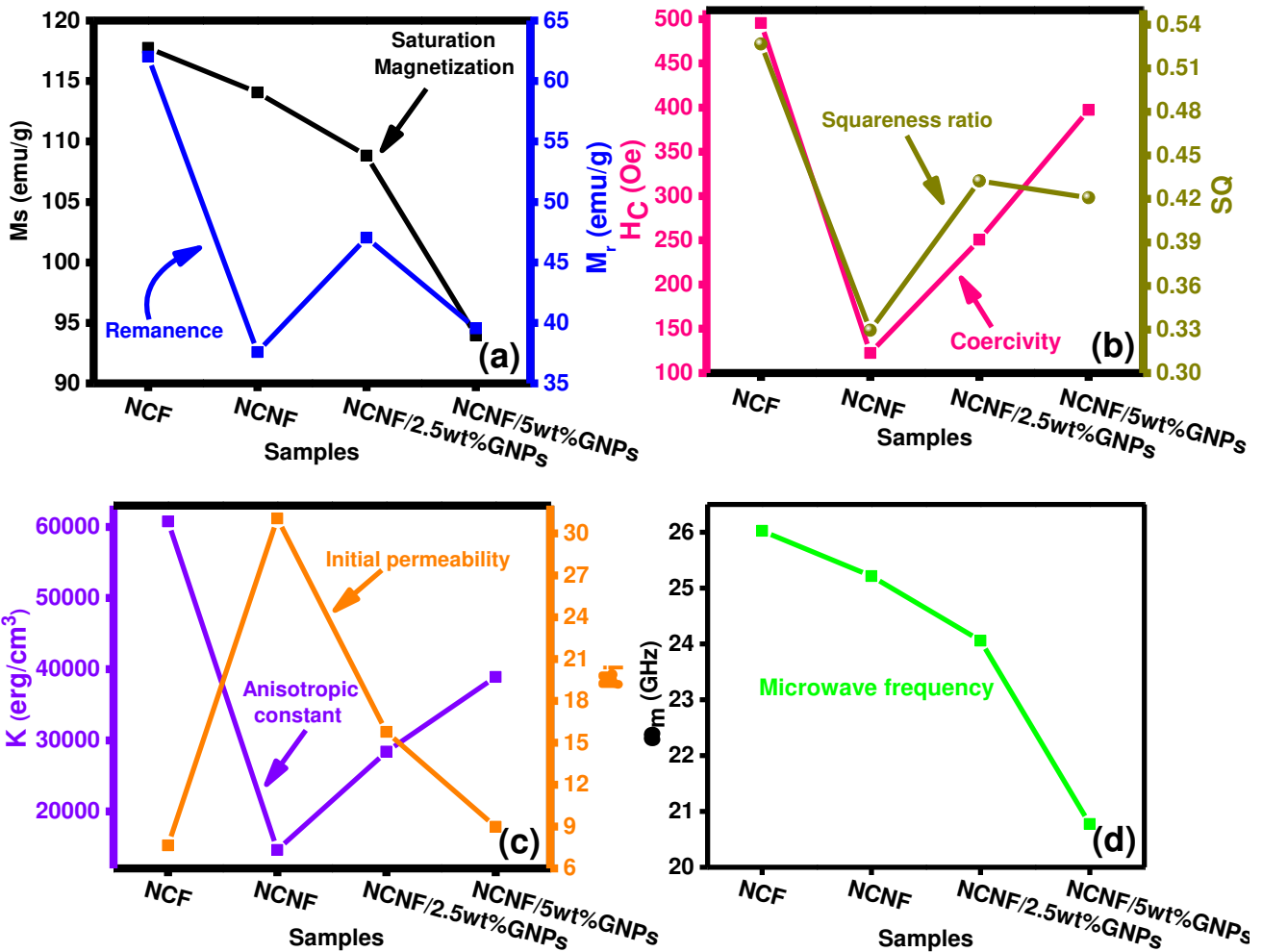**Fig. 21** Applied field *versus* microwave frequency for all the ferrites and composites

Fig. 22 Samples *versus* (**a**) saturation magnetization and remanence (**b**) coercivity (H_C), and squareness ratio (**c**) anisotropic constant and initial permeability (**d**) microwave frequency
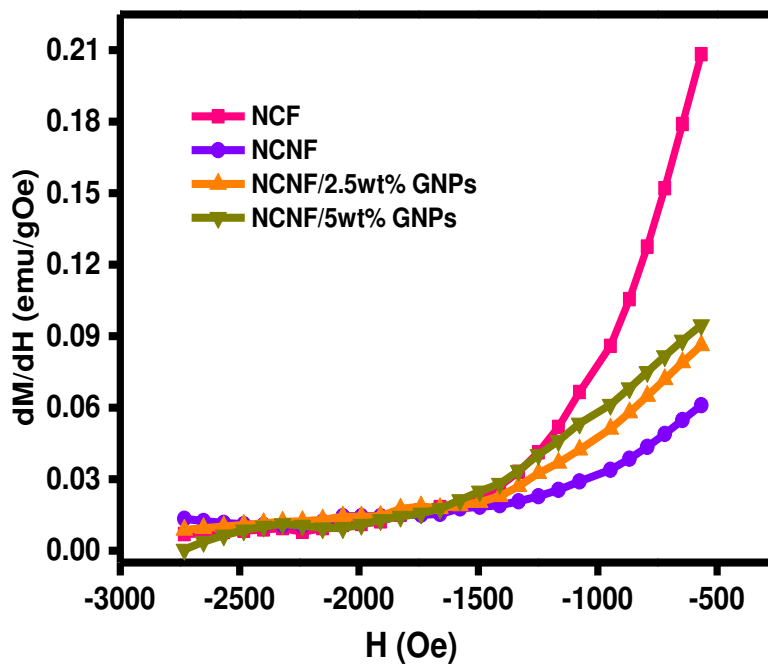

Fig. 23 Switching field distribution curves for all the ferrites and composites